Acta Biomaterialia 24 (2015) 172–192

Contents lists available at ScienceDirect

Acta Biomaterialia

journal homepage: www.elsevier.com/locate/actabiomat

# Biomechanical properties and microstructure of human ventricular myocardium

Gerhard Sommer [a,*], Andreas J. Schriefl [a], Michaela Andrä [b,c], Michael Sacherer [d], Christian Viertler [e], Heimo Wolinski [f], Gerhard A. Holzapfel [a]

[a] Institute of Biomechanics, Graz University of Technology, Austria
[b] Department of Surgery, Division of Transplantation Surgery, Medical University of Graz, Austria
[c] Division of Cardiothoracic and Vascular Surgery, Klinikum Klagenfurt am Wörthersee, Austria
[d] Department of Cardiology, Medical University of Graz, Austria
[e] Institute of Pathology, Medical University of Graz, Austria
[f] Institute of Molecular Biosciences, BioTechMed-Graz, University of Graz, Austria

ARTICLE INFO

*Article history:*
Received 16 February 2015
Received in revised form 12 May 2015
Accepted 24 June 2015
Available online 30 June 2015

*Keywords:*
Cardiac mechanics
Passive mechanical behavior
Biaxial extension testing
Triaxial shear testing
Microstructure
Second-harmonic generation
Optical clearing
Human ventricular myocardium

ABSTRACT

In the multidisciplinary field of heart research it is of utmost importance to identify accurate myocardium material properties for the description of phenomena such as mechano-electric feedback or heart wall thickening. A rationally-based material model is required to understand the highly nonlinear mechanics of complex structures such as the passive myocardium under different loading conditions. Unfortunately, to date there are no experimental data of human heart tissues available to estimate material parameters and to develop adequate material models. This study aimed to determine biaxial extension and triaxial shear properties and the underlying microstructure of the passive human ventricular myocardium. Using new state-of-the-art equipment, planar biaxial extension tests were performed to determine the biaxial extension properties of the passive ventricular human myocardium. Shear properties of the myocardium were examined by triaxial simple shear tests performed on small cubic specimens excised from an adjacent region of the biaxial extension specimens. The three-dimensional microstructure was investigated through second-harmonic generation (SHG) microscopy on optically cleared tissues, which emphasized the 3D orientation and dispersion of the myofibers and adjacent collagen fabrics. The results suggest that the passive human LV myocardium under quasi-static and dynamic multiaxial loadings is a nonlinear, anisotropic (orthotropic), viscoelastic and history-dependent soft biological material undergoing large deformations. Material properties of the tissue components along local microstructural axes drive the nonlinear and orthotropic features of the myocardium. SHG microscopy investigation revealed detailed information about the myocardial microstructure due to its high resolution. It enabled the identification of structural parameters such as the fiber and the sheet orientations and corresponding dispersions. With this complete set of material data, a sophisticated material model and associated material parameters can be defined for a better description of the biomechanical response of the ventricular myocardium in humans. Such a model will lead to more accurate computational simulations to better understand the fundamental underlying ventricular mechanics, a step needed in the improvement of medical treatment of heart diseases.

**Statement of Significance**

Unfortunately, to date there are no experimental data of human heart tissues available for material parameter estimation and the development of adequate material models. In this manuscript novel biaxial tensile and shear test data at different specimen orientations are presented, which allowed to adequately capture the direction-dependent material response. With these complete sets of mechanical data, combined with their underlying microstructural data (also presented herein), sophisticated material models and associated material parameters can be defined for the description of the mechanical behavior of the ventricular myocardium in humans. Such models will lead to accurate computational simulations to

* Corresponding author at: Institute of Biomechanics, Graz University of Technology, Kronesgasse 5/I, 8010 Graz, Austria.
*E-mail address:* sommer@tugraz.at (G. Sommer).

http://dx.doi.org/10.1016/j.actbio.2015.06.031

better understand the fundamental underlying ventricular mechanics, a step needed in the improvement of medical treatment of heart diseases.



## 1. Introduction

Heart related diseases are the leading cause of mortality in the world [1], and it is estimated that Europe alone spends about €196 billion per year on heart related medical treatments [2]. To better understand heart related diseases such as ventricular fibrillation, there is an acute need for more fundamental research to be carried out not only on cardiac electrophysiology but also on cardiac mechanics. The propagation of an electrical potential in the heart generates an active contraction determined by the underlying mechanical structure. On the other hand, changes in the lengths of myocytes influence the membrane potential and the duration of the action potential, a phenomenon known as mechano-electric feedback. Mechanics and electrophysiology are thus interlinked, and greater knowledge and insight into the behavior of the passive myocardium is of utmost importance to accurately capture the mechanical behavior of the heart and to better understand the mechanisms of the heart and its diseases as well as the development and the improvement of medical health care. For example, diastolic mechanical properties of cardiac muscles are important determinants of cardiac function with distinct passive myocardial stiffness contributing to diastolic heart failure [3]. Such ventricular diastolic dysfunction in patients with heart failure is associated with significant morbidity and mortality [4]. Hence, the passive stiffness of the myocardium is a major determinant of the overall cardiac function [5,6]. It is further suggested that shearing of adjacent muscle layers in the left ventricular wall contribute substantially to wall thickening during systole [7], and wall thinning during diastolic filling [8].

Modeling the cardiac function by using the finite element method has turned out to be a powerful task to increase the understanding of the physiological response of the heart and to determine how the structural components of the heart influence its behavior [9–14]. However, the development of realistic finite element models of the mechanical behavior of both healthy and diseased myocardial tissues is highly dependent on the formulation of appropriate constitutive laws and the accurate identification of their material parameters [15]. In particular, a better understanding of the fundamental underlying ventricular mechanics relies on: (i) realistic description of the three-dimensional geometry and microstructure of the myocardium including boundary conditions; (ii) constitutive equations that characterize the material properties of the myocardium [16].

Moreover, tissue engineered cardiac grafts are a promising therapeutic technique to repair injured hearts and to restore cardiac function after myocardial infarction [17]. In previous applications, tissue engineered patches were implanted over a region of infarcted cardiac tissue in order to stimulate angiogenesis and attenuate a reduction in cardiac function [18,19,17]. Since stem cells differentiate into different lineages depending on the mechanical properties of the matrix material [20], an appropriate biomechanical microenvironment for stem cells might lead to right differentiated cells [21]. Matching of the mechanical properties would enable tissue constructs to respond synchronically with heart contraction and relaxation and, therefore, allows efficient mechanical signal transfer from the native myocardial environment to the stem cells [22,21]. Hence, it is of importance to have an engineered cardiac patch that matches the mechanical properties of the native myocardium [22,17].

In the literature, the passive biaxial extension properties of the myocardium were documented [23–28], which mainly come from equibiaxial extension tests on hearts from mongrel dogs; only Yin et al. [24] performed 'true' biaxial extension tests with different ratios (as distinct from equibiaxial tests) on mongrel dogs, a study performed more than 25 years ago. The biaxial data of dog hearts indicate highly nonlinear and anisotropic properties. For myocardial tissues, these tests do not yield sufficient quantitative information to formulate a reliable constitutive law. In fact such data may even suggest that the material is transversely isotropic [29]. Myocardial tissue, however, is not transversely isotropic, which has been clearly demonstrated by the results of simple shear tests in different directions on the passive ventricular myocardium from porcine hearts [30]. These tests highlight the orthotropic behavior of myocardial tissue. Moreover, myocardial tissues undergo complex patterns of tensile, compressive, and, in particular, shear deformations throughout the cardiac cycle. Hence, data from biaxial tests alone are not enough to characterize the passive response of an orthotropic material such as the myocardium [16]. Prerequisites to capture the direction-dependent nonlinear material response involve a combination of biaxial extension test data with different loading protocols, and shear test data at different specimen orientations [16]. To the authors knowledge, no studies have been documented which conduct biaxial extension, triaxial shear, or a combination of these tests on human myocardial tissues.

From a microstructural viewpoint, it is known that muscle fibers are not perfectly aligned in the myocardial tissue [31]. Furthermore, the angular dispersion of the fibers is changing and is associated with several cardiac diseases, including dilated cardiomyopathy and familial hypertrophic cardiomyopathy [32,31]. There is only one study available where a mechanical model accounts for the dispersion of fibers and sheets in the myocardial tissue [14], but corresponding data for human myocardial tissue are missing. Multi-photon microscopy is well suited for the three-dimensional visualization of soft tissues due to its sequential automated slicing ability yielding *z*-stacks [33]. Nonlinear imaging techniques like second-harmonic generation (SHG) further allow for labeling free imaging of certain proteins including collagen and collagen-enclosed structures such as myocardial fibers. When utilized in combination with optical tissue clearing, greatly enhanced penetration depths can be achieved, allowing for an automated determination of orientation and dispersion parameters throughout thicker (>1 mm) tissue samples [34,35].

The aim of the present study is to characterize the mechanical properties of the passive human myocardium through biaxial extension and triaxial shear testing, and to determine the three-dimensional microstructure of the tested myocardium through a combination of optical clearing, SHG microscopy and subsequent 3D image analysis. The data stated in this study are intended to be used for the determination of new constitutive descriptors and its related parameters for more accurate computational studies of the fundamental mechanisms of human heart mechanics. Furthermore, the data stated can be used as a first standard mechanical and microstructural data set of the human ventricular myocardium, e.g., for the design and development of an optimal engineered cardiac construct for cardiac tissue repair.

## 2. Materials and methods

### 2.1. Materials

In total, human myocardial tissue from 28 subjects (11 women and 17 men) with an age of 61 ± 15 yrs (range 31–93) were tested. All myocardial samples were either excised within four hours after failed heart transplantation by the Clinical Department of Transplant Surgery, Medical University of Graz (MUG), Austria, or during autopsy within 12 h of death by the Institute of Pathology, MUG. The use of materials from human subjects was approved by the Ethical Committee at MUG with approval numbers 24–003 and 24–107. The commission assessed this research project based on the principles of the 'Declaration of Helsinki,' the 'ICH-GCP Guidelines,' and other laws that come into consideration to declare it as ethically inoffensive.

Myocardial tissue samples from 23 subjects were obtained from the Clinical Department of Transplant Surgery, when the donor-heart was not suitable for transplantation in terms of age, heart diseases, infections, etc., see Table 1. These hearts were arrested and inactivated during organ explantation by *in vivo* perfusion of 2000 ml cooled (4 °C, specified domain-temperature) cardioplegic solution CPS (Celsior by Genzyme Corporation) into cannulated coronary arteries. After explantation, the organ was inserted in 1000 ml CPS at 4 °C with dissolved 20 mM 2, 3-butanedione monoxime (BDM), which is known to inhibit cross-bridge activity and prevent contracture of the heart muscle [36,30]. BDM is a nucleophile agent which suppresses cardiac muscle contraction by inhibiting myosin-light-chain reactions with actin. Mainly, parts of the left ventricular free wall (LVFW) or the interventricular wall (IVW, septum) could be obtained. Rarely, parts from all regions, LVFW, IVW, and the right ventricular free wall (RVFW) of the myocardium could be obtained, see Fig. 1. The Institute of Pathology provided five human hearts that were excised during autopsy within 12 h after death. The extracted samples were stored in cooled CPS.

Anamneses of all donors including age, gender, primary disease, cause of death, echocardiographic parameters, cardiovascular treatments, risk factors were recorded, see Table 1. Both the relatively high number of specimens and the anamneses of the donors served to achieve statistically meaningful results and, moreover, easier and descriptive interpretations of these classified results.

### 2.2. Methods

This study is accomplished in three steps: (i) 'true' planar biaxial extension tests were performed to determine the biaxial properties of human ventricular myocardium; (ii) triaxial shear properties in all three orthogonal orientations were determined by simple shear tests on three cubic specimens taken from a region adjacent to the biaxially tested specimens; (iii) the microstructure of the tested specimens was determined through multi-photon microscopy on optically cleared tissue samples.

#### 2.2.1. Biaxial extension testing

*Specimen preparations.* For the preparation of thin myocardial slices with homogeneous thickness and a smooth surface, an

**Table 1**
Patient information of all investigated specimens (*I–XXVIII*), corresponding heart wall thicknesses, echocardiographic parameters, heart related diseases, risk factors, and reasons for transplantation refusal of the heart. Tissue from hearts *II, III, IV, XIII, and XXVII* were received from the Institute of Pathology.

| Heart no. | LVFW (mm) | IVW (mm) | Echocardiography | | | Heart related diseases/Risk factors | Patient information | | | | Reason for refusal |
|---|---|---|---|---|---|---|---|---|---|---|---|
| | | | LVEDD (mm) | E/A | EF (%) | | Age (yrs) | Sex | BMI (kg/m$^2$) | Cause of death | |
| *I* | 19 | 22 | 54 | 1 | 55 | HYP, HTN, CD | 75 | m | 33 | TBI | Age |
| *II* | 13 | 14 | – | – | – | CS, SEMI | 77 | f | 21 | SEMI | – |
| *III* | 16 | 18 | – | – | – | HYP | 32 | f | 22 | – | – |
| *IV* | 18 | 19 | – | – | – | CS, MI, HYP | 93 | f | 21 | SEMI | – |
| *V* | 13 | 15 | norm | – | – | LVDD I, low MR | 40 | m | 26 | SDH | MAL |
| *VI* | 7 | 10 | – | – | – | AIVS, LVD | 31 | f | 22 | TBI | LVD |
| *VII* | 7 | 8 | 39 | 0.63 | 60 | – | 70 | f | 22 | SDH | Age |
| *VIII* | 12 | 14 | 38 | 0.6 | – | LVDD II, high MR | 71 | f | 27 | – | Age |
| *IX* | 11 | 11 | 40 | 0.72 | 60 | abnormal ECG | 62 | f | 24 | CVB | MED |
| *X* | 10 | 11 | 51 | 0.68 | 65 | possible MI | 57 | m | 26 | HIE | CPR |
| *XI* | 9 | 9 | norm | – | 65 | slight AIVS | 66 | f | 23 | SDH | MAL |
| *XII* | 10 | 10 | – | – | 58 | HTN, low MR | 57 | f | 22 | SAH | MED |
| *XIII* | 11 | 12 | – | – | – | RCC | 56 | m | – | CE | – |
| *XIV* | 11 | 11 | 39 | 1.4 | 84 | HYP, borderline PAP | 57 | f | 29 | ASAH | Age |
| *XV* | 18 | 16 | 37 | 0.61 | 72 | HYP, UHD, DM | 73 | m | 27 | TBI | Age, MS |
| *XVI* | 9 | 7 | – | – | – | HoTN, SMO, AA | 72 | m | 28 | – | MED |
| *XVII* | 9 | 10 | – | – | >60 | MI, SMO, AA | 48 | m | 21 | ICH + SAH | CPR |
| *XVIII* | 11 | 12 | 44 | 0.8 | 60 | MI, DM | 62 | m | 26 | STRA | MED |
| *XIX* | 16 | 12 | 42 | >1 | 65 | HTN | 71 | m | 25 | ICH | MED |
| *XX* | 14 | 14 | 37 | 0.8 | 55 | SSS, AF, CAD, HTN, SMO | 71 | f | 28 | SAH | MED |
| *XXI* | 8 | 10 | 40 | – | 60 | SMO, AA | 39 | m | 28 | SDH | – |
| *XXII* | 16 | 18 | 48 | 1.5 | 64 | HTN, SMO | 49 | m | 34 | MEN, SAH | MED |
| *XXIII* | 13 | 13 | 38 | 0.62 | 65 | HTN | 69 | m | 32 | SDH | MED |
| *XXIV* | 8 | 8 | 42 | 0.56 | 60 | CAD | 63 | m | 26 | ICH | MED |
| *XXV* | 11 | 9 | 48 | – | 70 | – | 75 | m | 25 | SAH | MED |
| *XXVI* | 11 | 17 | 40 | – | 65 | – | 43 | m | 24 | TBI | CPR |
| *XXVII* | 17 | 16 | – | – | – | – | 60 | m | 25 | MEN | – |
| *XXVIII* | 21 | 14 | 35 | <1 | 60 | – | 74 | m | 25 | – | Age |

AA, alcohol abuse; AF, atrial fibrillation; AIVS, akinetic interventricular septum; ASAH, aneurysmal subarachnoid hemorrhage; BMI, body mass index; CAD, coronary artery disease; CD, cardiac dysrythmia; CE, cerebral edema; CPR, cardiopulmonary resuscitation; CS, coronary sclerosis; CVB, cardiovascular bleeding; DM, diabetes mellitus; E/A, ratio of the early (E) to late (A) ventricular filling flow velocities; ECG, electrocardiogram; EF, ejection fraction; HIE, hypoxic ischemic encephalopathy; HoTN, hypotension; HTN, hypertension; HYP, hypertrophy; ICH, intracerebral hemorrhage; IVW, interventricular wall thickness; LVD, left ventricle dysfunction; LVDD x, left ventricle diastolic dysfunction of grade x; LVEDD, left ventricle end-diastolic diameter; LVFW, left ventricle free wall thickness; MAL, malignity; MED, medical reasons; MEN, meningitis; MI, myocardial infarction; MR, mitral regurgitation; MS, metabolic syndrome; norm, normal; PAP, pulmonary artery pressure; RCC, renal cell carcinoma; SAH, subarachnoid hemorrhage; SDH, subdural haemorrhage; SEMI, subendocardial myocardial infarction; SMO, smoker; SSS, sick sinus syndrome; STRA, strangulation trauma; TBI, traumatic brain injury; UHD, unstable hemodynamics; –, unknown or not determined.

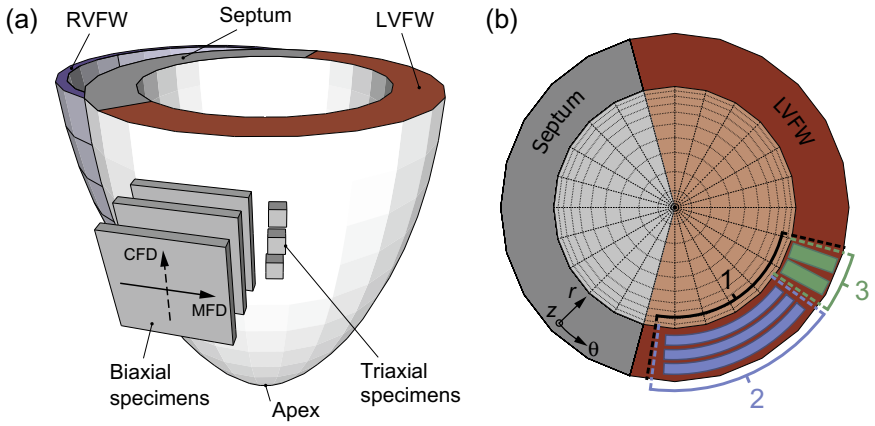


**Fig. 1.** (a) 3D schematic model of the human ventricular myocardium composed of the right ventricular free wall (RVFW), the septum, and the left ventricular free wall (LVFW). Typically, squared biaxial and cubic triaxial specimens were obtained from the anterior site of the LVFW; (b) top view of the left ventricle with locations for specimen preparations. The red-colored region identifies the LVFW. The black dashed region (1) shows a typical myocardium sample received from the departments. In the blue region (2), possible slices for the preparation of squared biaxial extension specimens are represented, while the green region (3) indicates possible slices for the preparation of cubic triaxial shear specimens. The local coordinates $\theta, r$ and $z$ correspond to the circumferential, radial and axial directions of the 'ellipsoidal' ventricles, respectively. (For interpretation of the references to color in this figure legend, the reader is referred to the web version of this article.)

electrical universal cutter was used. From these thin slices, squared specimens with the dimensions of $25 \times 25$ mm were prepared with one side aligned with the mean-fiber direction (MFD) and the other in the cross-fiber direction (CFD) [37]. Several suitable specimens were extracted throughout the myocardial wall from the epicardium to the endocardium. An effort was made to obtain suitable specimens from the outer, the middle and the inner portion of the wall. 'Outer' corresponds to specimens taken $\sim 1.5$–2.0 mm below the epicardial surface, 'middle' means within the middle-third of a wall, and 'inner' specimens were taken close to the subendocardium, just below the deepest invagination of the endocardial surface.

For a detailed description of the preparation method for suitable biaxial specimens, the reader is referred to the preliminary study [37]. Finally, the specimen was mounted with surgical suture material cords to the carriages of the testing setup in a trampoline fashion and submerged in a bath of CPS with 20 mM BDM, which was kept at 37 °C during the entire biaxial extension tests, see Fig. 2. It is crucial to perform mechanical experiments on passive cardiac tissues at sufficient high temperatures (>25 °C) or in the presence of an inhibitor of cross-bridge cycling, like BDM [38]. Additionally to CPS, the authors used both body temperature (37 °C) and BDM to ensure passiveness of the cardiac muscle.

*Biaxial extension protocol.* Different stretches (5–20% in 2.5% increments) were applied consecutively, starting at the lowest stretch and continuing until the tissue fails. For each stretch level, four preconditioning cycles and one measuring cycle were performed at different loading ratios (1(MFD):1(CFD), $1:0.75, 1:0.5, 0.75:1, 0.5:1$). In turn, each measuring cycle is composed of a loading and an unloading curve. It is crucial to apply different loading ratios between MFD and CFD in order to capture the direction-dependent material response by biaxial extension testing with a higher resolution. Moreover, this so-called 'true' biaxial testing approach covers a large range of deformations of the tissue and, therefore, leads to a unique set of constitutive parameters for the tested specimen. During the tests, the forces from the loadings cells, the position of the carriages, and the distance between the markers were recorded and used for data analysis. The authors observed that the results were very sensitive to the initial preloads. In order to obtain reproducible results, a

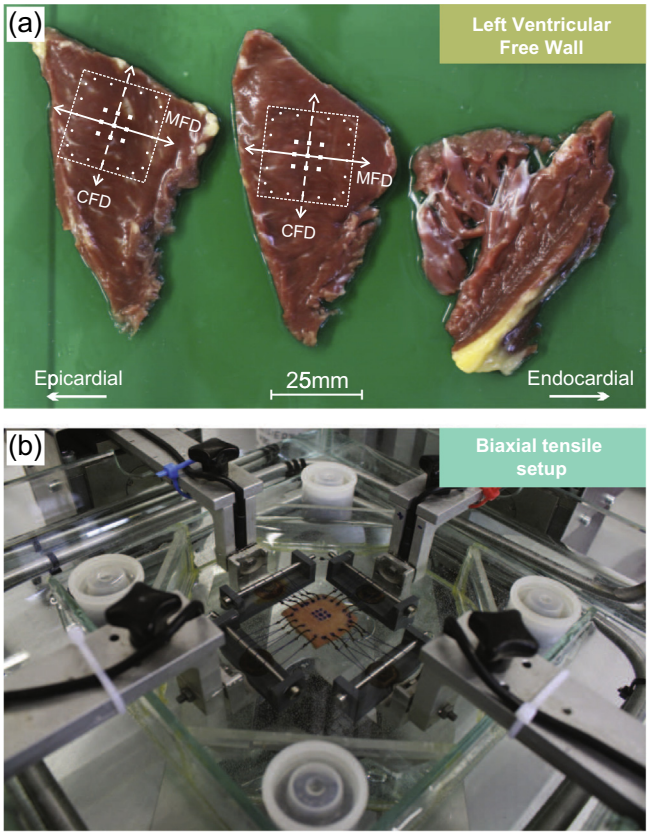


**Fig. 2.** Preparation of a squared specimen for biaxial extension testing with sides aligned with the MFD and CFD. In panel (a), three slices through the myocardial wall are shown. The slices in (a) correspond to the myocardium close to the epicardium (left), the middle region of the myocardium (middle), and the myocardium close to the endocardium (right). The location of extraction of a biaxial testing specimen with a side length of 25 mm is indicated by a dashed square. White dots and squares indicate positions for hooks and deformation markers, respectively. Panel (b) shows a squared myocardial specimen inserted in the biaxial extension rig, which is ready for testing. Additionally, linear actuator arms, submergible load cells, and the heated container filled with CPS and BDM are visible.

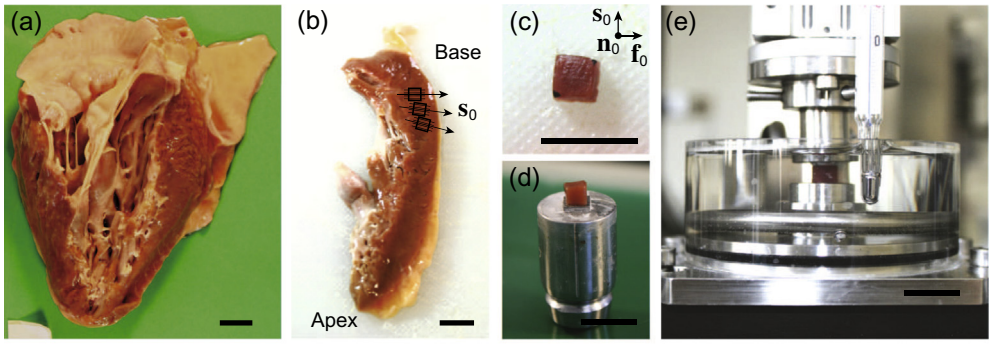


**Fig. 3.** Preparation of a cubic specimen for triaxial shear testing with sides aligned to the principal material axes: (a) typical left ventricular sample obtained from the Institute of Pathology; (b) transmural base-apex segment (thickness $\sim 5$ mm) sliced from the LV sample with an electric universal cutter. Additionally, the locations for extraction of three cubic specimens and the corresponding sheet directions $\mathbf{s}_0$, indicated by arrows, are sketched in (b); (c) representative myocardial cube with $\sim 4$ mm side length with its sides aligned with the fiber $\mathbf{f}_0$, sheet $\mathbf{s}_0$, and sheet-normal $\mathbf{n}_0$ directions; (d) cubic specimen glued to the upper specimen holder of the triaxial testing setup ready for insertion in the testing setup; (e) specimen inserted in the setup ready for testing. Additionally, the 3-axes-load cell (top), the heating element, and the container filled with CPS with BDM (center) are visible in panel (e). The black scale bars in each picture indicate a length of 10 mm.

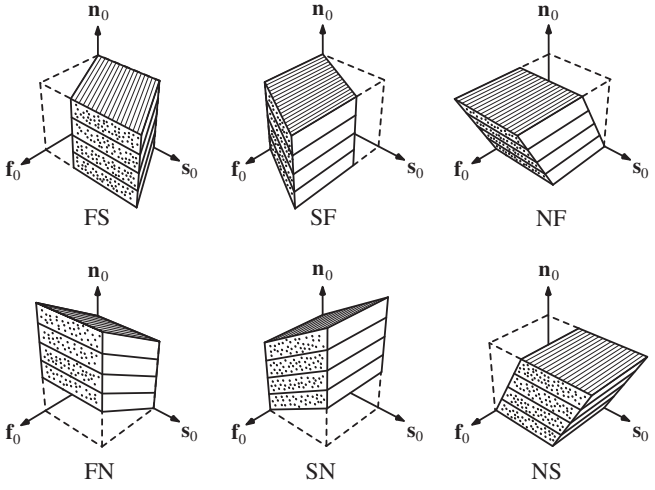


**Fig. 4.** Six possible simple shear modes for an orthotropic myocardium cube defined with respect to the fiber $\mathbf{f}_0$, sheet $\mathbf{s}_0$, and sheet-normal direction $\mathbf{n}_0$. The modes are $ij$ and $i,j \in$ {F,S,N}, where $i$ denotes the normal vector of the face that is shifted by the simple shear and $j$ denotes the direction in which the face is shifted.

prestress of 0.1 kPa in terms of engineering stress (corresponds to $\sim 5$ mN) to each specimen was applied. To account for viscoelastic features of the tissue, relaxation tests (Cauchy stresses vs. time) at a ramp speed of 100 mm/min for the stretch level of 10% and a duration of 5 min were conducted.

However, biaxial extension tests alone are not able to formulate an exact mechanical description of an orthotropic material such as the myocardium [29]. Moreover, LeGrice et al. [7] claimed that there is evidence that relative sliding of myocardial layers is responsible for the left ventricular ejection by contributing to subendocardial wall thickening during systole. This is similar to wall thinning that occurs during passive ventricular filling, which is associated with reorientation or shearing of myocardial layers. Hence, biaxial extension tests are complemented (enhanced) by triaxial shear testing on cubic myocardial specimens.

### 2.2.2. Triaxial shear testing

*Specimen preparations.* On the basis of the local laminar architecture of the myocardium, the authors can define a right-handed orthogonal set of axes at every material point within the ventricular wall, which relate to: the myofiber direction or fiber axis (F), the direction transverse to the fiber axis within the layer or sheet axis (S), and the direction perpendicular to the fibers and layers or sheet-normal axis (N), obtaining an FSN-coordinate system (see Fig. 1 in [30] or [16]). Due to the local variations of the muscle fiber and sheet directions in the myocardium [39], the obtained cubic specimen should be as small as possible. In this study, we were able to prepare cubic specimens from the left ventricular wall with an edge length of $\sim 4$ mm (Fig. 3) and with sides aligned to the principal axes FSN, see Fig. 4. Unfortunately, the wall of the right ventricle was too thin to prepare an appropriate cubic specimen for triaxial shear testing. In order to obtain suitable specimens, an assessment of appropriate regions in the heart with uniformly aligned fibers and layers is very important. For example, such regions can be found in the LVFW at about one-third of the distance from base to apex [30,39]. In this region, the orientation of muscle sheets in the transmural plane is $\sim 45°$ to the base, and the fibers are oriented in the circumferential direction of the left ventricle and, therefore, perpendicular to transmural plane, see also Fig. 1 in [30]. Transmural base-apex segments were first sliced with an electric universal cutter to achieve smooth, uniformly thick slices of $\sim 5$ mm. From the slices made, a region with parallel sheet-layers was selected. For easier structural identification, Evans blue dye was used to highlight the laminar structure [30]. Subsequently, slices were incised parallel to sheets using a trimming blade. The remaining columnar specimens (4 mm width, 4 mm thick) were truncated at 4 mm to achieve cubic specimens with $\sim 4 \times 4 \times 4$ mm. Specimen dimensions were measured before and after the tests using a micrometer. The specimen was then glued to the upper specimen holder and inserted in the triaxial shear testing device (Fig. 3).

The specifications of the used device are described in detail elsewhere [40]. In brief, the operation principle involves affixing the tissue specimens to both the upper and lower platforms, using a thin layer of cyanoacrylate adhesive and bathed in a tempered solution at $\sim 37$ °C (Fig. 3). The lower platform is moved relative to the fixed upper platform using a biaxial translation stage.

*Triaxial shear protocol.* Shear testing was performed under quasi-static conditions ($v = 1$ mm/min) in CPS with BDM. The solution's temperature was maintained at 37 °C by a heater circulation unit for suitable conditions during testing. Three cycles (two for preconditioning and one for further data analysis) of sinusoidal simple shear (0.1–0.5 in 0.1 increments of specimen thickness) were subsequently applied to the specimens in two orthogonal directions. Consequently, for the six possible modes of simple shear for an orthotropic material, three specimens were needed. For a depiction of the possible shear modes, see Fig. 4. Resulting

forces in the three axes $(x, y, z)$ were measured. In preliminary tests, we observed an asymmetry in the shear properties between positive and negative amount of shear. This was due, in part, to small relative shear displacements on the upper to lower surfaces of the specimen during mounting. This residual shear was minimized through offset correcting by small displacements of the lower platform. Displacements of $< 10\%$ of the specimen thickness were necessary in order to obtain almost symmetric shear properties.

On completion of shear testing, relaxation tests ('step test') at an amount of shear of 0.5 were performed for all six shear modes in order to account for the viscoelastic properties of the tissue. Therefore, a rapid shear step to 0.5 'amount of shear' was imposed and the resultant forces were recorded for 300 s.

After the completion of testing, all specimens were carefully examined for evidence of unwanted penetration of glue into the specimen or along its unattached sides. All mechanical tests were finished within 24 h after excision from the body.

### 2.2.3. Microstructural Investigations

*Nonlinear optical imaging.* All tissue samples utilized for microstructural investigations via SHG imaging were from adjacent regions of specimens, which underwent biaxial and triaxial mechanical testing. Before imaging, the specimen were optically cleared using a 1 : 2 solution of benzyl alcohol: benzyl benzoate to enhance the SHG penetration depth, following the clearing protocol documented in [35]. A myocardial specimen before and after optical clearing is depicted in Fig. 5. SHG-imaging of cardiac muscle fibers was performed using an imaging-setup consisting of a picosecond laser source and an optical parametric oscillator (OPO; picoEmerald; APE; Germany; HighQ Laser, Austria) integrated into a Leica SP5 confocal microscope (Leica Microsystems, Inc., Mannheim, Germany). To enable SHG inducing of collagen, the OPO was tuned to 880 nm. For the detection of the second-harmonic signal, a BP 465/170 emission filter in combination with a nondescanned detector in epi-mode (backward detection) was used. The images were acquired using a Leica HCX IRAPO L $25 \times 0.95$ water objective with a working distance of 2.5 mm for deep tissue imaging. The resulting image ($z$-) stacks are comprised of two-dimensional images recorded from the previously cleared specimen, and each stack contains sectional images with a field of view of $620 \times 620$ µm in the $(x, y)$-plane. In depth ($z$-direction), step sizes are consistent in each recorded stack but vary between $0.4, 5, 10$ and 20 µm. A representative 2-D image obtained via SHG can be seen in Fig. 6. The $x$ and $y$-directions in Figs. 15 and 18 coincide with the MFD and CFD of the biaxial specimens, respectively, whereas the $z$-direction coincides with the radial direction of the ventricles (see Fig. 1). Furthermore, the $(x, y)$-plane in Figs. 15 and 18 corresponds to the circumferential-axial $(\theta, z)$-plane of the ventricles (Fig. 1).

Image processing of $z$-stacks and subsequent volume-rendering were performed using the software package AMIRA (FEI Visualization Sciences Group, Bordeaux, France and Zuse Institute Berlin, Germany). Prior to the actual volume rendering, several different image filters such as Gaussian filtering, and unsharp masking, amongst others, were applied to improve the overall outcome.

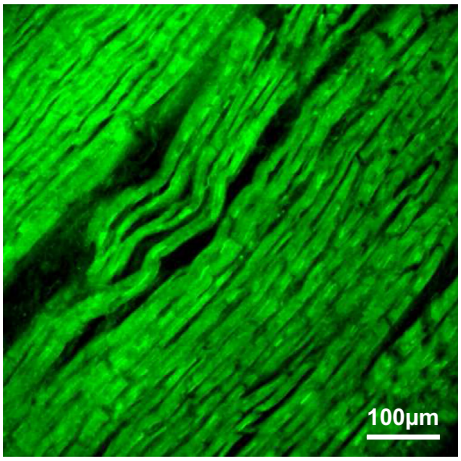


**Fig. 6.** Representative example of a SHG image of heart muscle fibers with a field of view of $620 \times 620$ µm. The myocyte structure is highlighted in light green, where endo and perimysial collagen is visible in green or dark green. The image reveals that heart muscle fibers run mainly parallel in the aged but 'healthy' human left ventricular myocardium.

## 2.3. Data analysis

### 2.3.1. Biaxial extension response

The Cauchy stress $\sigma$ and the stretch $\lambda$ were computed and plotted against each other. The assumption of negligible shear components was justified in a previous study [37]. In that study during biaxial testing, nine markers on the surface of the specimens were tracked using a differential digital image tracking algorithm and shear stresses vs. normal stresses were evaluated. Peak shear stress to normal stress ratios were determined to be lower than 1%, if no severe damage occurred in the tissue [37]. Therefore, the approach with sides aligned in the MFD and CFD provide results with negligible shear deformations and shear stresses.

With the incompressibility assumption [23], the (normal) Cauchy stresses in MFD, $\sigma_{11}$, and CFD, $\sigma_{22}$, can be determined from the conveniently obtainable first Piola–Kirchhoff stresses in MFD, $P_{11}$, and CFD, $P_{22}$, respectively [41]. Thus,

$$\sigma_{11} = \lambda_1 P_{11} = \lambda_1 \frac{f_1}{TL_2}, \qquad \sigma_{22} = \lambda_2 P_{22} = \lambda_2 \frac{f_2}{TL_1}, \tag{1}$$

where $\lambda_1 = x_1/X_1$ and $\lambda_2 = x_2/X_2$ represent the tissue stretches in each direction based on the marker distances in the loaded $(x_1, x_2)$ and unloaded $(X_1, X_2)$ configuration. The measured forces in each direction are denoted as $f_1$ and $f_2, T$ is the mean thickness in the

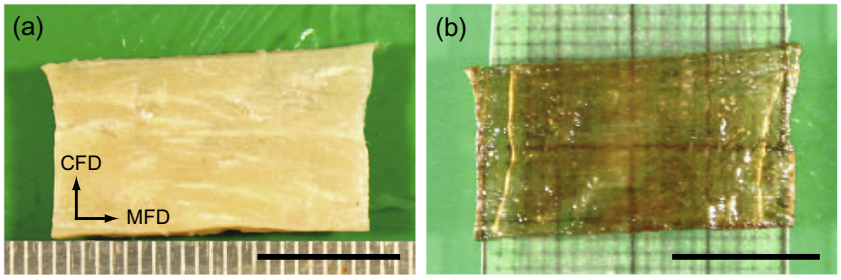


**Fig. 5.** Formaldehyde fixed myocardial specimen with a thickness of $\sim 2.5$ mm for microstructural investigation before (a) and after (b) dehydration and optical clearing. MFD and CFD correspond to the long and short axis of the rectangular specimen, respectively. The black scale bar indicates 10 mm.

unloaded reference configuration, and $L_1$ and $L_2$ are the measurable side-lengths of the specimen in the undeformed state in the fiber and cross-fiber direction, respectively. In our case, $L_1$ and $L_2$ were approx. 25 mm.

#### 2.3.2. Triaxial shear response

'Amount of shear' and corresponding shear stresses were computed to quantify the triaxial shear response of the myocardial tissue cubes. In general, for simple shear, the 'amount of shear' $\gamma$ is defined as the relative in-plane displacement of two parallel layers in a material body divided by their separation distance. Here, $\gamma$ ranges from 0.1 to 0.5 in increments of 0.1, and the separation distance is the side-length of the specimen cube $L \sim 4$ mm. For simple shear, the shear stress $\tau$ is defined as the ratio of shear force $f$ to shear area $a = L^2$. In particular, $\gamma$ and $\tau$ are given as

$$\gamma = \frac{\Delta l}{L}, \qquad \tau = \frac{f}{L^2}, \tag{2}$$

where $\Delta l$ denotes the shear displacement.

#### 2.3.3. Fiber orientation and dispersion quantification from SHG imaging

Fiber orientations were extracted from 3D images ($z$-stack) using a Fourier-based image analysis method in combination with wedge filtering [34,35]. The resulting fiber dispersions throughout the in-plane thickness ($x,y$-plane) and the out-of-plane sheet dispersion ($x,z$-plane) of the tissue were fitted using Least Squares Fitting (LSF) with a $\pi$-periodic von Mises distribution, yielding (i) the location parameter $\mu$ describing the principle (or preferred) orientation of a given distribution as a function of depth and (ii) the concentration parameter $b$ describing the shape (or alignment) of a given distribution as a function of depth. High $b$ values correspond to a narrow shape of the fitted function (thus, a more anisotropic cardiac muscle fiber distribution) while low $b$ values ($< 1$) correspond to less fiber alignment (a more isotropic fiber distribution). Additionally, the dispersion parameter $\kappa$ (nonlinearly dependent on $b$) was determined, because it can be directly utilized for computational modeling. Values for $\kappa$ can range between 0 and 1/3, with $\kappa = 0$ corresponding to a perfect fiber alignment ($b \longrightarrow \infty$) and $\kappa = 1/3$ corresponding to a completely isotropic fiber distribution ($b = 0$) [42,35].

#### 2.3.4. Statistical analyses

Statistical analyses were performed to test for significant correlations between different patient-specific data (i.e. age, ejection fraction, E/A ratios) and mechanical data (i.e. peak Cauchy stress values in MFD and CFD) using Pearson's correlation coefficient. Moreover, we tested for statistical differences of the mechanical properties between different regions in the myocardium, i.e. between LVFW, septum, and RVFW, between epicardial and endocardial sites, and between basal and apical sites using paired two-sample $t$-test. $p$-values were determined based on Student's $t$-distribution, where $p < 0.05$ was considered to be significant. Statistical analyses were performed using the OriginLab ORIGIN 7.5 program package. All data values are presented as mean values (mean) ± standard deviation (SD).

## 3. Results

### 3.1. Anamnesis, geometry

In Table 1, heart related parameters (wall thicknesses, echocardiographic parameters, etc.) and anamneses (heart related diseases/risk factors, age, sex, BMI, cause of death, etc.) of 28 subjects *I–XXVIII* were documented. Since such factors may affect the mechanical properties of cardiovascular tissues [43], they should be taken into account in a complete registration of myocardial mechanics. The age of the subjects ranged from 31 to 93 yrs with a mean age of 61 ± 15 yrs. The mean heart weight was determined as 341 ± 89 g. The average thicknesses of the LVFW and the septum lie with 13 ± 4 mm in the normal to hypertrophic range. Especially the hearts *I, IV* and *XXVIII* with wall thicknesses of 18–22 mm were clearly hypertrophic. The mean ejection fraction value of 65 ± 7% indicates normal systolic function, while the mean E/A ratio of 0.9 ± 0.3 reveals slightly impaired diastolic ventricular function of the heart. Ejection fractions of 55–70% and $E/A > 1$ were defined to be normal. We found a strikingly negative correlation between age and E/A ratio of $R = -0.6$ ($p = 0.05$). No significant correlations were found between age and ejection fraction ($R = -0.1, p = 0.79$) or between E/A ratio and ejection fraction ($R = 0.4, p = 0.23$).

Load-free in-plane dimensions of the biaxial specimens were always approx. 25 × 25 mm and the central region wherein stress and strain were calculated was approx. 5 × 5 mm, only 4% of the total planar area. The thicknesses varied from 1.5 to 3.5 mm with an average thickness of 2.3 ± 0.8 mm ($n = 56$). The average dimensions for height and width of all considered myocardial cubes ($n = 170$) for the triaxial shear tests were determined to be 3.9 ± 0.8 and 4.0 ± 0.7, respectively.

### 3.2. Biaxial extension behavior

A representative (quasi-static) equibiaxial mechanical response, in terms of the Cauchy stress vs. the stretch, of the preconditioned myocardial specimen *XXVII* subjected to stretch levels ranging from 1.05 to 1.15, in increments of 0.025 is shown in Fig. 7(a). The myocardium revealed pronounced nonlinear, highly anisotropic, and viscoelastic behavior (hysteresis formation) with a stiffer behavior and larger hysteresis in the mean-fiber direction (MFD) than in the cross-fiber direction (CFD). Average hysteresis areas or dissipation energy per unit volume (absolute values and relative values regarding the area below the loading curve) for different stretch ratios (1(MFD): 1(CFD), $1:0.75, 0.75:1, 1:0.5, 0.5:1$) are summarized in Table 2. In particular, the average hysteresis areas in MFD and CFD obtained by equibiaxial testing at 10% stretch were computed to be 91 J/m$^3$ and 52 J/m$^3$, respectively. These values correspond to a hysteresis area percentage relative to the area under the loading curve of 37.5% for both the MFD and CFD, see Table 2.

A typical preconditioning behavior (specimen *XXVII*) during equibiaxial loading at stretch levels of 7.5% and 10% is depicted in Fig. 7(b), which was consistent in all tested specimens. For clarity, only the first, fourth, and fifth cycles are plotted. The curves were stable and repeatable after a few preconditioning cycles, in particular three to four cycles were enough to preconditioning the human myocardium. During preconditioning, the change of the maximum stress value from cycle to cycle was very small almost not evident, but a notable decrease of the hysteresis area was observed, see Fig. 7(b). Softening between subsequent stretch levels was clearly visible in the human myocardium. The main softening occurred in the first cycle when the stretch level was increased, as clearly evident in Fig. 7(b), resulting in different (softer) preconditioned material properties for each increased stretch level.

For the stretch level of 10% the Figs. 7(c) and (d) show a representative (specimen *XXVII*) and an average ($n = 26$) 'true' biaxial extension test behavior, with different stretch ratios between MFD and CFD. The 'true' biaxial testing protocol is important because it provides data for the 'cross-coupling' of stresses. As can be seen in Figs. 7(c) and (d), remarkable cross-talk between MFD and CFD is supported by the five distinct curves that are

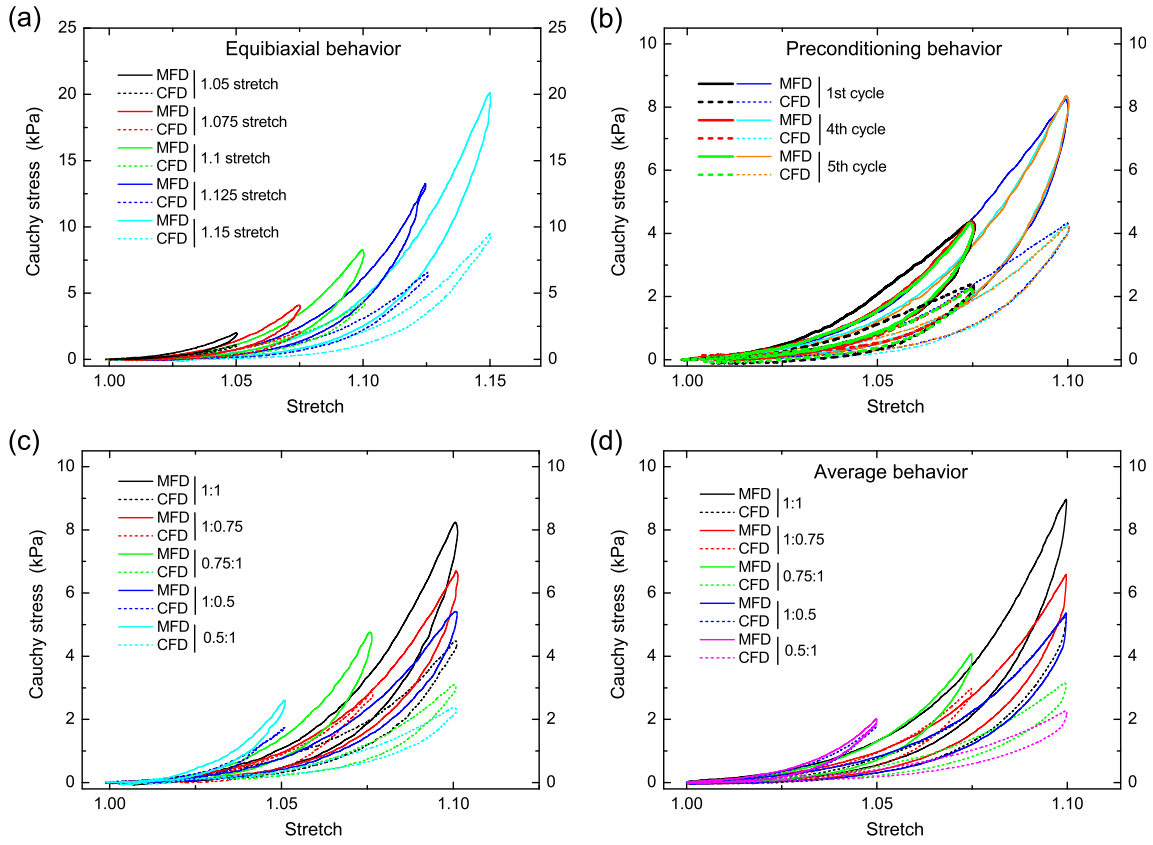


**Fig. 7.** Representative (specimen *XXVII*) and average passive biaxial Cauchy stress vs. stretch behavior in the MFD (solid curves) and CFD (dashed curves) of human LVFW specimens: (a) typical preconditioned equibiaxial properties at subsequently increased stretch levels ranging from 1.05 to 1.15 in 0.025 increments; (b) representative preconditioning behavior in terms of first, fourth, and fifth loading–unloading cycles at two subsequent stretch levels (7.5 and 10%); (c) typical 'true' biaxial behavior, i.e. at different ratios between MFD and CFD ($1:1, 1:0.75, 0.75:1, 1:0.5$, and $0.5:1$), is depicted for a stretch level of 10%; (d) average behavior of biaxial specimens ($n = 26$) tested at a max. stretch of 10% and for all five stretch ratios.

recorded in each stress-stretch plane as a result of the five loading protocols. Interestingly, similar Cauchy stress-stretch behavior of MFD and CFD was obtained when the tissue was subjected to a loading ratio of MFD:CFD $= 1:0.75$, see the red curves in the Fig. 7(c), (d).

Viscoelastic behavior of the tissue during biaxial testing is clearly visible, see Fig. 8. Stresses and hystereses increase with increased actuator speed for a typical specimen *IX*, see Fig. 8(a). Maximum stresses increased about 7% from normal testing speed (3 mm/min) to about 3-times higher speed (10 mm/min), and increased about 19% from normal to 10-times higher speed (30 mm/min). Average (equibiaxial) stress relaxation behavior (Cauchy stresses vs. time) of five specimens for a duration of 5 min is shown in Fig. 8(b). The most drastic relaxation was observed within the first 5 mins, but specimens continued to relax up to 30 min (not shown herein). After 5 min, stress relaxation percentages of 41% in MFD and 45% in CFD were determined.

Although the myocardial behavior is well represented in Fig. 7, specimen-to-specimen variations have been observed, and, therefore, the average biaxial Cauchy stress-stretch behavior obtained from all considered myocardial specimens ($n = 26$) for a stretch level of 10% was computed and plotted in Fig. 9. Therein, only the average between the loading and the unloading path is presented. It should be mentioned that the average between the two paths is assumed to be the elastic tissue behavior as the strain rate approaches to zero for which the hystereses vanish. For simplicity we subsequently refer to the average between the two paths as the 'elastic' tissue behavior. Fig. 9(a) shows the average 'elastic' behavior of all tested specimens at different ratios between MFD and CFD ($1:1, 1:0.75, 0.75:1, 1:0.5$, and $0.5:1$), where Figs. 9(b)–(f) present mean values and corresponding standard deviation values indicated as error bars.

Different regions of ventricular myocardium (LVFW, septum, RVFW, equatorial or apical, epicardial or endocardial) revealed similar qualitative properties (nonlinearity, anisotropy, hysteresis formation, etc.). In order to allow a quantitative comparison between different regions, peak Cauchy stresses (mean ± SD) of equibiaxially tested myocardial tissues were computed at different stretch levels. In Table 3, peak Cauchy stresses obtained from LV, LVFW, septum, and RVFW are summarized. For clarity, the values in Table 3 are also presented as column plots in Fig. 10. For the LVFW, the septum, and the RVFW, similar ratios of peak Cauchy stresses in MFD and in CFD of 1.9, 1.8, and 1.7, respectively, were obtained. This indicates an approximately twice as stiff material in MFD than in CFD. For different stretch levels (1.05–1.15), no significant differences in peak Cauchy stresses between LVFW and septum ($p = 0.45$) were obtained. However, RVFW revealed significantly higher peak stress values than LVFW ($p = 0.009$) and septum ($p = 0.022$) for stretch levels larger than 1.075 (see Table 3 or Fig. 10). Furthermore, no significant differences in peak Cauchy stresses in specimens obtained from the epicardial or endocardial site of the LV ($p = 0.49$) were observed. This indicates similar mechanical properties throughout the myocardial ventricular wall.

In comparison with patient specific parameters, we found a significant positive correlation ($R = 0.9, p = 0.04$) between E/A ratios and peak Cauchy stress values in MFD. We further obtained a decreased stiffness (peak Cauchy stress values) with increasing age ($R = -0.3$), but this correlation was not significant ($p = 0.41$). Furthermore, no significant correlation ($R = -0.2, p = 0.65$) was

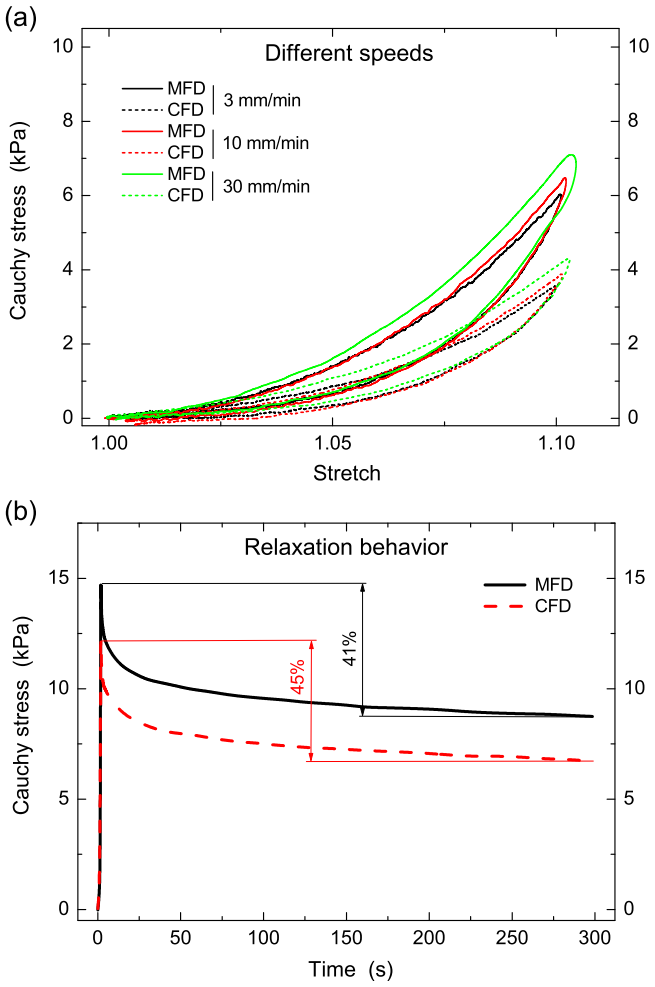


**Fig. 8.** Viscoelastic biaxial extension properties of the human myocardium: (a) typical equibiaxial behavior at the three different speeds of 3, 10, and 30 mm/min and a stretch level of 10% of specimen *IX*; (b) average ($n = 5$) stress relaxation behavior at 10% stretch during a duration of 5 mins. MFD and CFD are indicated by solid and dashed curves, respectively.

found between ejection fraction and mechanical properties of the passive myocardium.

### 3.3. Triaxial shear behavior

Representative results for all six modes of simple shear (FS, FN, SF, SN, NF, NS) for three adjacent specimens from donor *XXI*, each exposed to subsequently applied 'amount of shear' ($\gamma = 0.1$–$0.5$), are displayed in Fig. 11. The modes FS and FN showed remarkably higher shear stresses at equivalent amounts of shear than the other four modes. In general, triaxial shear properties of the passive ventricular myocardium were nonlinear, viscoelastic, and dependent on the cardiac myofibers and sheets, which manifest the orthotropic nature of the myocardial tissue. The stiffness along the three axes increases as follows: N (sheet-normal direction) < S (sheet direction) < F (fiber direction). Strain softening was observed for all shear modes. To quantify this softening, slopes at a specific stress level for the subsequently applied shear levels ($0.2, 0.3, 0.4, 0.5$) were computed. The decrease in slope was similar for all shear modes, e.g., a slope decrease of 30–35% from shear level 0.2 to 0.4 was observed.

Representative preconditioning behavior during simple shear testing (donor *XXI*), in terms of shear stress vs. amount of shear, in which three cycles (two preconditioning and one measurement cycles) of sinusoidal shear deformation at two subsequent shear amplitudes of 0.4 and 0.5 were applied in the FS-mode, see Fig. 12(a). The typical preconditioning behavior was observed in all specimens, i.e. the stress and the hysteresis were always larger on the initial shear deformations in positive and negative directions than in subsequent cycles. After only two cycles, shear stress vs. amount of shear loops were reproducible. One can see in Fig. 12(a), as the amount of shear was increased, the first loading cycle of the new stress–strain curve followed the preconditioned loading curve of the preceding cycle. For a given shear level, the relative extent of softening was similar for each shear mode. Similar to the biaxial extension testing, the softening during preconditioning of the passive myocardium during triaxial shear testing appears to be irreversible, inelastic and dependent on the strain history (Mullins effect).

Hysteresis formation was pronounced, indicating significant energy dissipation of the myocardium during cyclic shearing. Even at a very low speed of $v = 0.1$ mm/min (equivalent to $\sim 40$ min/cycle), the observed hysteresis area did not vanish and was still remarkable (not shown herein). Average hysteresis areas (mean $\pm$ SD) for all different shear modes and at different shear levels are summarized in Table 4 and Fig. 12(b). For all shear modes, the hysteresis area increased with increasing shear level. Within each shear level, no significant differences between the shear modes were found. However, at a shear level of $\gamma = 0.5$ slightly higher hysteresis areas were obtained in the FS mode in comparison with FN ($p = 0.51$), SF ($p = 0.45$), and SN ($p = 0.50$) modes, while the hysteresis of mode FS was strikingly higher in comparison with modes NF ($p = 0.07$) and NS ($p = 0.06$), see also Fig. 12(b). Viscoelastic properties during shearing are evident from the average stress relaxation behavior of all six shear modes after a simple shear step of $\gamma = 0.5$, as illustrated in Fig. 12(c). The stress drop after 300 s relaxation was found to be greater than 50%. Corresponding relaxation behavior was observed in all specimens.

Analogous to the biaxial extension behavior, the 'elastic' shear behavior (the mean curve of the loading and unloading curves) was computed for each shear direction and shear level. In Fig. 13, the mean 'elastic' curves and corresponding SD (error bars) of all considered specimens are plotted for the shear levels 0.2 ($n = 24$), 0.3 ($n = 23$), 0.4 ($n = 23$), and 0.5 ($n = 18$). The mean curves of the six shear directions at different shear levels reveal shear anisotropy and strain softening. Corresponding peak shear stress values (mean $\pm$ SD) for each shear mode and the shear levels 0.2 ($n = 24$), 0.3 ($n = 23$), 0.4 ($n = 23$), and 0.5 ($n = 18$) are summarized in Table 5. For easier interpretation, these values are also illustrated in terms of column plots in Fig. 14. Although SD values indicate some variation in absolute values of peak stresses between hearts, differences between shear modes were consistent between experiments. The difference between the FS and FN-modes and the other four modes increased with increasing amount of shear. In particular, significant differences between FS,FN and SF,SN,NF,NS-modes for the amount of shear values of 0.4 ($p < 0.02$) and 0.5 ($p < 0.01$) were observed. However, for smaller amounts of shear values ($0.2, 0.3$), significant differences were only obtained between the shear modes FS and FN, and NF and NS, i.e. $p < 0.05$ for $\gamma = 0.2$ and $p < 0.02$ for 0.3, respectively. No significant differences were observed within pairs, i.e. between FS- and FN-, or SF- and SN-, or NF- and NS-modes ($p > 0.50$). This behavior suggests that shear properties of the human left ventricular myocardium are orthotropic with highest resistance to shear in the FS and FN-modes, intermediate in the SF and SN-modes, and lowest in the NF and NS-modes.

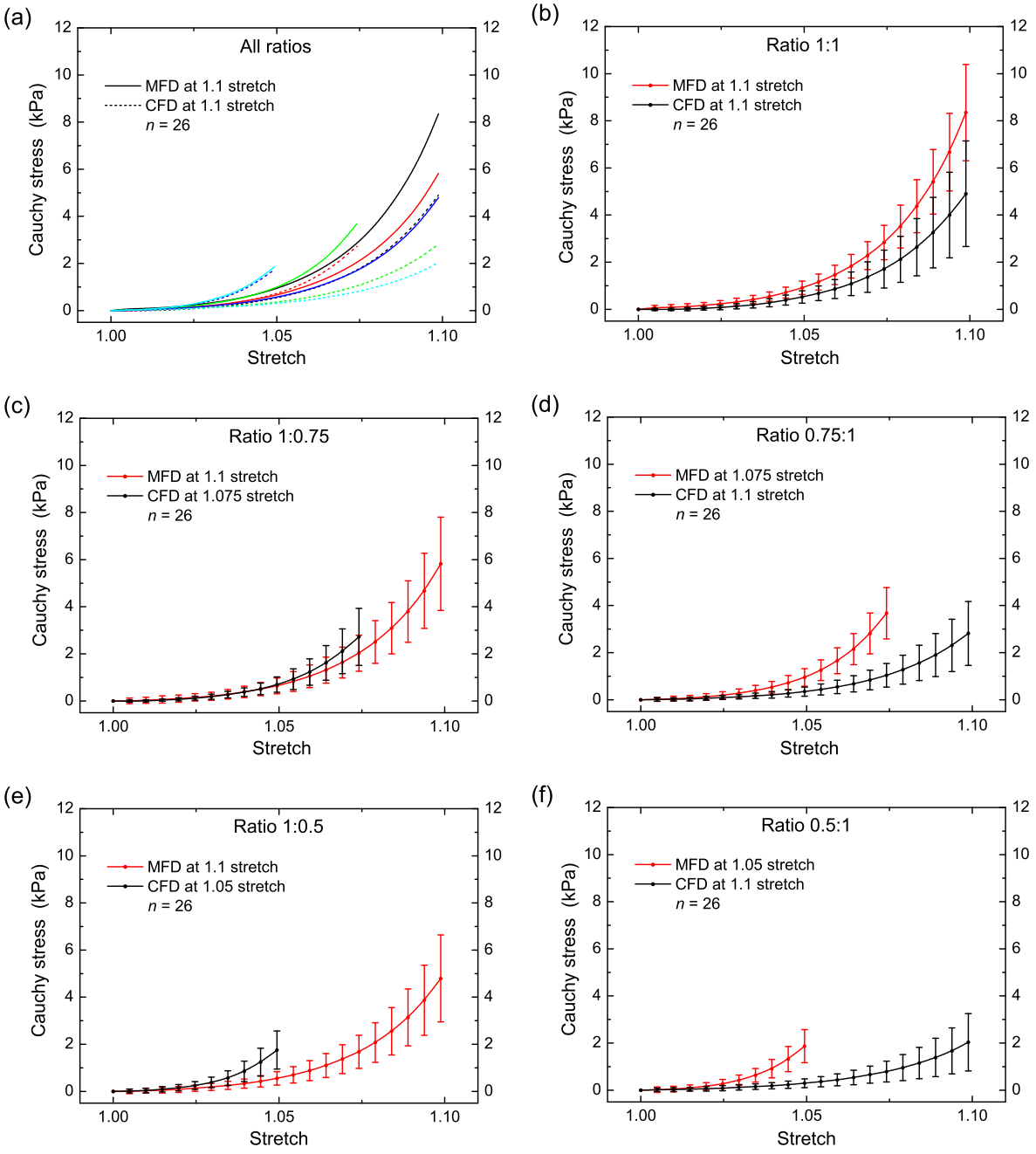


**Fig. 9.** Average 'elastic' biaxial Cauchy stress vs. stretch behavior of all considered human LV myocardial specimens ($n = 26$) subjected to a max. stretch of 10% with different stretch ratios between MFD and CFD: (a) different stretch ratios, where black curves correspond to $1:1$, red to $1:0.75$, green to $0.75:1$, blue to $1:0.5$ and cyan to $0.5:1$; (b)–(f) mean curves and corresponding standard deviations indicated by error bars for the stretch ratios $1:1, 1:0.75, 0.75:1, 1:0.5$, and $0.5:1$, where red and black curves correspond to the mean fiber direction (MFD) and the cross-fiber direction (CFD), respectively. (For interpretation of the references to color in this figure legend, the reader is referred to the web version of this article.)

### 3.4. Microstructural analysis

Image stacks ($z$-stacks) obtained via SHG imaging are presented as volume-rendered 3D projections. In Fig. 15 a representative 3D reconstruction of an image stack showing a depth of 985 μm with in-plane $(x, y)$-dimensions of $620 \times 620$ μm is depicted. Straight fibers that run parallel align to form sheets. In this 3D reconstruction individual sheets several fibers thick can be observed. Note that the dark discontinuities appearing in the $(x, z)$-plane, dividing individual sheets, are most likely cleavage planes. According to the literature [39], sheets are 3–4 cells wide, while the sheets observable in this 3D reconstruction seem to exceed this width. The intensity plot in Fig. 16 represents the typical three-dimensional in-plane $(x, y)$ muscle fiber orientations through-the-thickness of approx. 1200 μm with colors ranging from dark blue (0%) to dark red (100%), reflecting relative changes in amplitudes. Preferred fiber directions appear in red, while blue areas indicate the presence of few to no fibers.

In total, 28 specimens, which were (mainly) obtained from the left ventricle wall, from different locations (either endocardial, medial or epicardial), were used to identify the change of fiber orientations and its dispersion through the ventricular wall. From LSF,

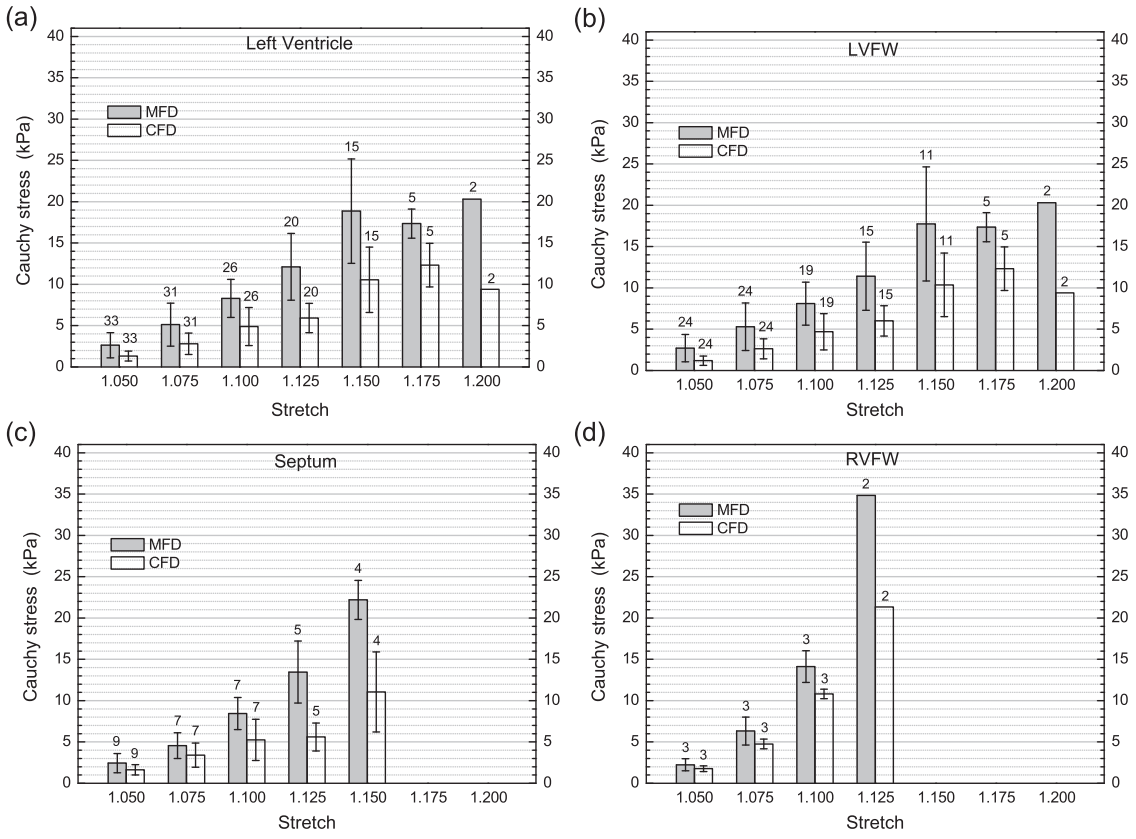


**Fig. 10.** Column plots of the peak Cauchy stresses (mean ± SD) at subsequent increased stretch levels (1.05, 1.075, 1.1, 1.125, 1.15, 1.175, 1.2) obtained from passive equibiaxial extension tests in the MFD (gray columns) and the CFD (white columns) of the human myocardium: (a)–(d) maximum Cauchy stresses of all considered specimens for the left ventricle, LVFW, septum, and RVFW, respectively. Error bars indicate corresponding standard deviation values. The number of specimens considered are mentioned above each column. Values are also stated in Table 3.

both the location parameter $\mu$ and the concentration parameter $b$ were obtained and calculated for every single image in the $z$-stack, where $\mu$ corresponds to the most red parts in the intensity plots, see Fig. 16. The corresponding coefficient of determination $R^2$, a measure of the goodness of fit, was determined for each image and plotted over the depth. While a value of $R^2 = 1$ indicates perfectly fitted data, $R^2 > 0.8$ were satisfactory and respective data were considered for further evaluations. Fig. 17 illustrates the different parameters (location parameter $\mu$, concentration parameter $b$, coefficients of determination $R^2$, and additionally the dispersion parameter $\kappa$) over the depth of a representative $(x,y)$-stack (sample *XIII*).

Mean value and standard deviation (mean ± SD) were calculated for all considered $(x,y)$-stacks of different specimens ($n = 21$) resulting in an average in-plane fiber rotation of $\bar{\phi} = 14.8 \pm 6.9^{\circ}$ per mm depth. A corresponding mean concentration parameter $\bar{b} = 4.5 \pm 1.7$ was determined, while the dispersion parameter exhibits on average $\bar{\kappa} = 0.08 \pm 0.03$. Outliers were determined based on the interquartile range rule and not considered for the mean and SD calculations.

Selective samples were imaged in the $(x,z)$-plane to visualize the out-of-plane muscle fiber orientation. A representative sample is illustrated in Fig. 18, where in (a) a projection in the $(x,z)$-plane of the rotated sample is depicted, and in (b) the 3D reconstruction of the $(x,z)$-stack with 660 μm depth and a slice distance of 0.4 μm is shown. A typical intensity plot of the out-of-plane $(x,z)$ fiber orientation shown in Fig. 19 reveals that only a few fibers are oriented in the radial ($z$-) direction, but, instead, are organized in sheets. After recording and processing the $(x,z)$-stacks, fibers running out-of-plane could be identified. The slight change of orientation throughout the depth of 600 $\mu$m can be observed in Fig. 20(a) demonstrating the location parameter $\mu$ plotted over the respective depth. The corresponding concentration parameter $b$, dispersion parameter $\kappa$, and coefficient of determination $R^2$ over the depth are plotted in Fig. 20(b)–(d).

The results arising from these stacks vary slightly between the different $(x,z)$-stacks of the specimens ($n = 3$) yielding a mean out-of-plane rotation of $\bar{\phi} = 3.5 \pm 2.0^{\circ}$ per mm depth, a mean concentration parameter $\bar{b} = 3.9 \pm 1.0$ leading to a dispersion parameter of $\bar{\kappa} = 0.11 \pm 0.03$.

## 4. Discussion

The development of realistic computer models for the mechanical behavior of soft biological tissues in health and disease is dependent on the formulation of appropriate constitutive laws and an accurate identification of material properties. As stated by Holzapfel and Ogden [16], the problem in developing an adequate constitutive model is the shortage of experimental data suitable for detailed parameter estimation in specific functional forms, and, therefore, there is a pressing need for more data to inform further development based on the framework discussed in their work. Therefore, the novel combination of biaxial extension and shear testing, together with the investigation of the microstructure, of the passive human ventricular myocardium will be able to analyze the capability of existing constitutive models. Furthermore, this combination will yield new innovative and essential information about material properties to fulfill the short term goals of constructing realistic myocardial models capable of capturing the mechanics of the heart as well as aiding the long term goals of

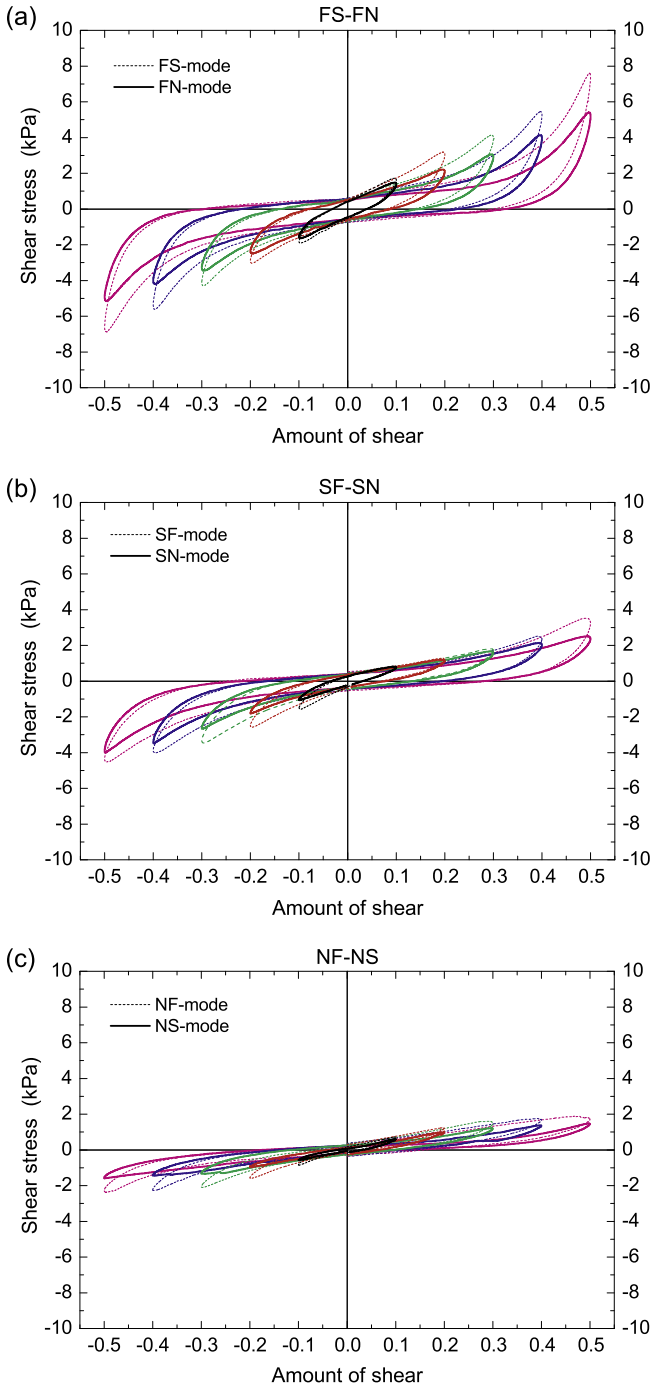


**Fig. 11.** Representative passive shear stress vs. 'amount of shear' behavior during final cycles of sinusoidal simple shear deformations for human myocardial specimens from heart *XXI* subjected to six shear modes: (a) FS- and FN-modes; (b) SF- and SN-modes; (c) NF- and NS-modes. Maximum amount of shear is progressively increased from 0.1 to 0.5, in increments of 0.1. Data reveal anisotropy, pronounced hysteresis formation, and strain softening at increased amount of shear.

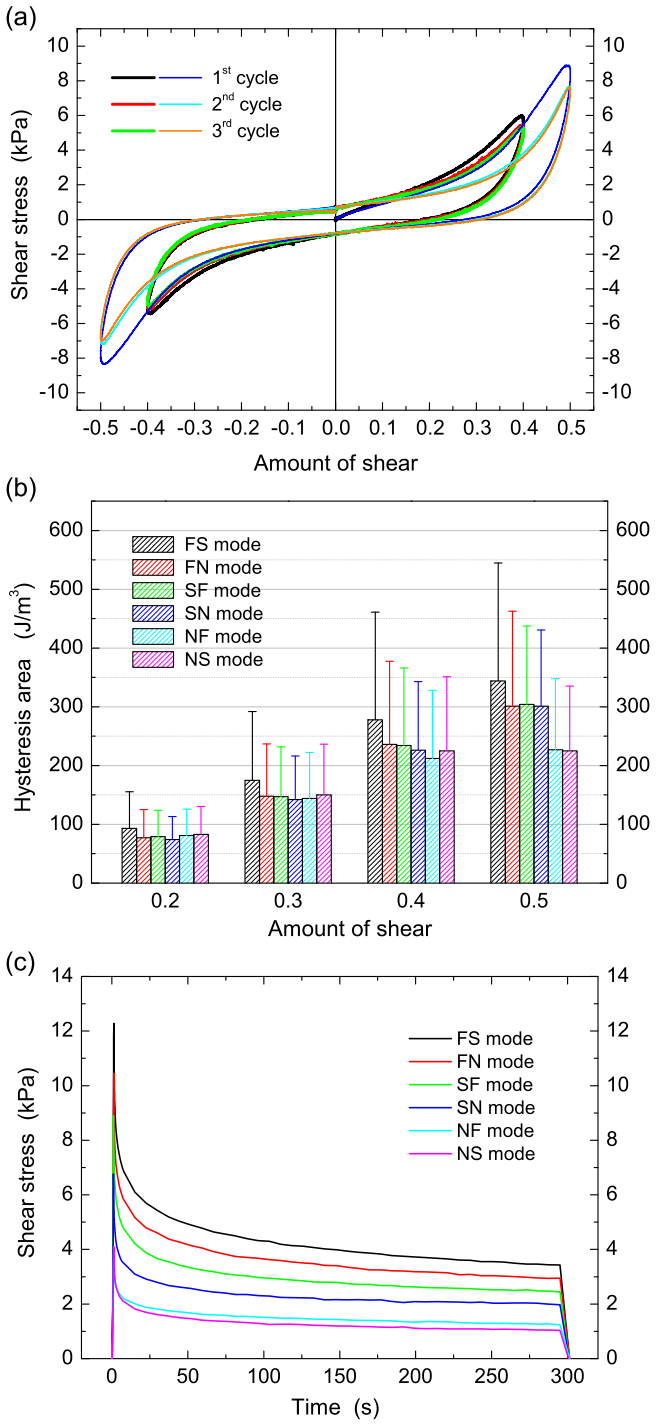


**Fig. 12.** Preconditioning, hysteresis area, and relaxation behavior during simple shear testing of human myocardium: (a) representative preconditioning behavior (donor *XXI*) during three sinusoidal simple shear cycles for two subsequent shear levels (0.4 and 0.5) in FS-mode; (b) column plots reveal average hysteresis areas (mean ± SD) for all shear modes at different shear levels (0.2, 0.3, 0.4, 0.5); (c) average ($n = 5$) relaxation behavior (shear stress vs. time) at an amount of shear of $\gamma = 0.5$ for all shear modes, FS (black), FN (red), SF (green), SN (blue), NF (cyan) and NS (magenta). Relaxation tests were conducted for a duration of 300 s. (For interpretation of the references to color in this figure legend, the reader is referred to the web version of this article.)

improving methods of medical treatment and quality of life for people suffering from heart diseases. The use of classified human heart tissues according to the anamneses of the donors will have an important impact to help understand or identify a population, and, therefore, has clinical clear relevance. To the best of the authors' knowledge, this study represents the first biaxial extension and triaxial shear measurements of the passive human myocardium.

### 4.1. Biaxial extension behavior

Under biaxial extension, all tissue specimens of the passive human ventricular myocardium experienced large deformations, revealed highly nonlinear, anisotropic stress-stretch relationship

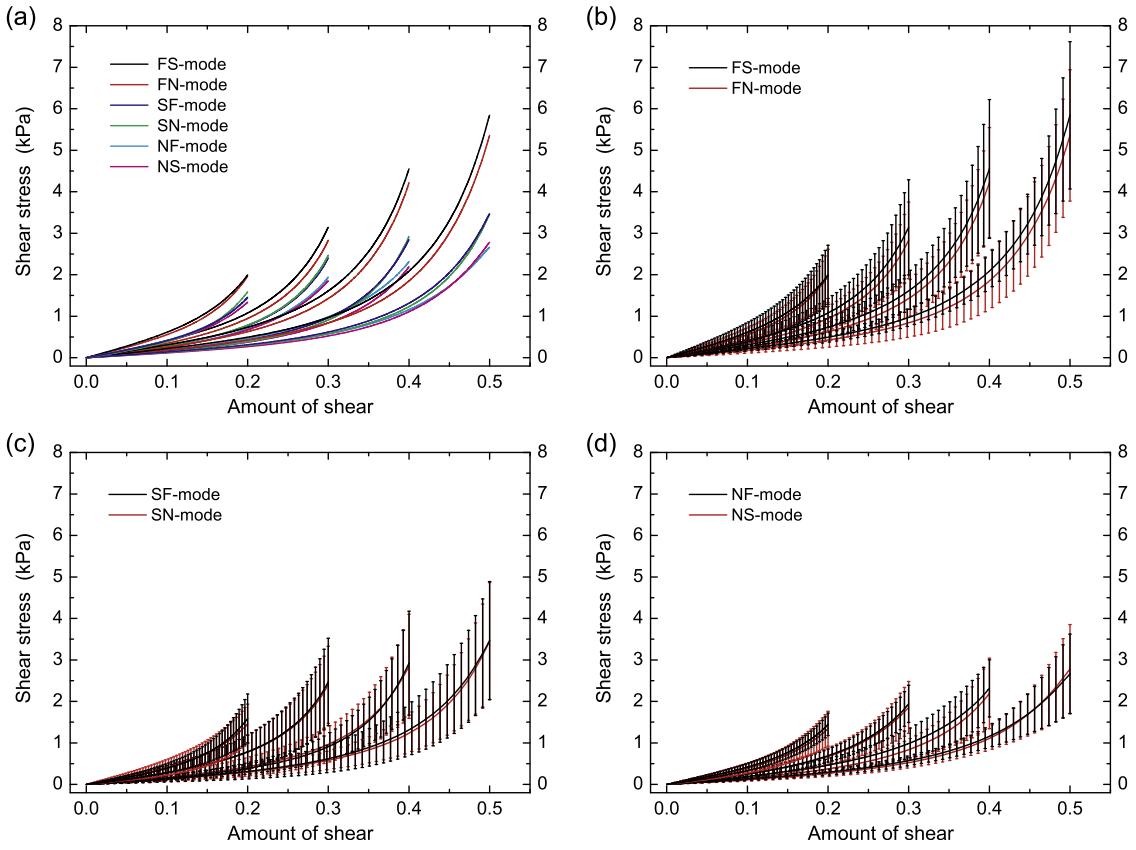


**Fig. 13.** Average 'elastic' triaxial shear stress vs. 'amount of shear' behavior of all considered human myocardial specimens subjected to each shear mode (FS, FN, SF, SN, NF, NS) at 'amount of shear'-levels of 0.2 ($n = 24$), 0.3 ($n = 23$), 0.4 ($n = 23$), and 0.5 ($n = 18$): (a) all shear modes are incorporated, where black curves correspond to FS-, red to FN-, green to SF-, blue to SN-, cyan to NF-, and magenta to NS-mode; (b)–(d) mean curves and corresponding standard deviations by means of error bars for the shear modes FS,FN, SF,SN, and NF,NS, respectively. (For interpretation of the references to color in this figure legend, the reader is referred to the web version of this article.)

and the formation of a pronounced hysteresis with stiffer behavior and larger hysteresis in MFD than in CFD. Large deformations, nonlinear stress-stretch behavior, anisotropy, and small hysteresis are commonly exhibited by many biological tissues [44–46,40,47]. However, the passive cardiac muscle showed pronounced hysteresis, indicating a significant energy dissipation during quasistatic cyclic loading. On average, we observed a bigger absolute hysteresis area for MFD (91 J/m$^3$) than for CFD (52 J/m$^3$); however, they were similar relative to the areas below the loading curves (38%), see Table 2.

In order to yield repeatable measurement results, four preconditioning cycles were executed prior to every measurement cycle. As Fig. 7(b) shows, the number of repetitions was sufficient for our tests. During cyclic biaxial preconditioning of the passive human ventricular myocardium, the main part of the mechanical softening with decreasing hysteresis occurs during the first two preconditioning cycles, where after three to four cycles the tissue revealed stable and reproducible biaxial behavior. Preconditioning cycles used for biaxial testing of animal myocardial tissue (mainly canine, one bovine, and one murine) ranged from 5–7 [24,25,48,49] and to 7–10 [26,27,50–53], where five [26,27] for canine and seven for bovine myocardium [51] were stated to be enough.

Softening of the passive human myocardium seems to be irreversible and occurs whenever the load increases beyond its prior all-time maximum value. This stress-softening behavior is also known as Mullins effect [54]. The major part of the softening occurred during the first loading beyond the previous stretch level to the next stretch level, see Fig. 7(b). Due to the softening of the passive human myocardium, we observed different (preconditioned) material properties at different stretch levels. Similar softening behavior has been observed in cyclic inflations of intact passive hearts of rats [55–57]. The authors argued that this strain softening was caused by disruption of perimysial collagen due to excessive shearing between adjacent myocardial muscle layers at elevated levels of LV inflation [55]. Strain softening in the passive LV myocardium may also be explained by stretch-dependent damage to the endomysial collagen [58], or changes in the collagen matrix, where the myocytes are embedded [59]. Alternatively, disruption of myofilaments (such as titin, actin and myosin) or of cytoskeletal proteins may be involved in strain softening of the passive myocardial tissues [60,61].

In order to obtain data for the 'cross-coupling' of stresses in anisotropic materials, biaxial extension testing with different ratios between MFD and CFD or 'true' biaxial extension testing is essential. The equibiaxial extension loading condition of the myocardium is only a special (short-term) condition during the cardiac cycle and, therefore, very rarely experienced by the tissue *in vivo*. Hence, it is crucial to apply different loading ratios between MFD and CFD in order to capture the direction-dependent material response with a higher resolution. Moreover, the used 'true' biaxial testing protocol covers a large range of deformations of the tissue and will lead to a unique set of constitutive parameters for the biaxially tested specimens. The passive human myocardium showed a strong mechanical coupling between MFD and CFD, which is evident in the separated solid and dashed curves of the Figs. 7(c), (d) and 9. For example, if there is no mechanical coupling between MFD and CFD in human myocardium, the three solid curves at 10% stretch would be coincident. Interestingly, for a loading ratio of MFD:CFD $= 1 : 0.75$, we observed similar Cauchy

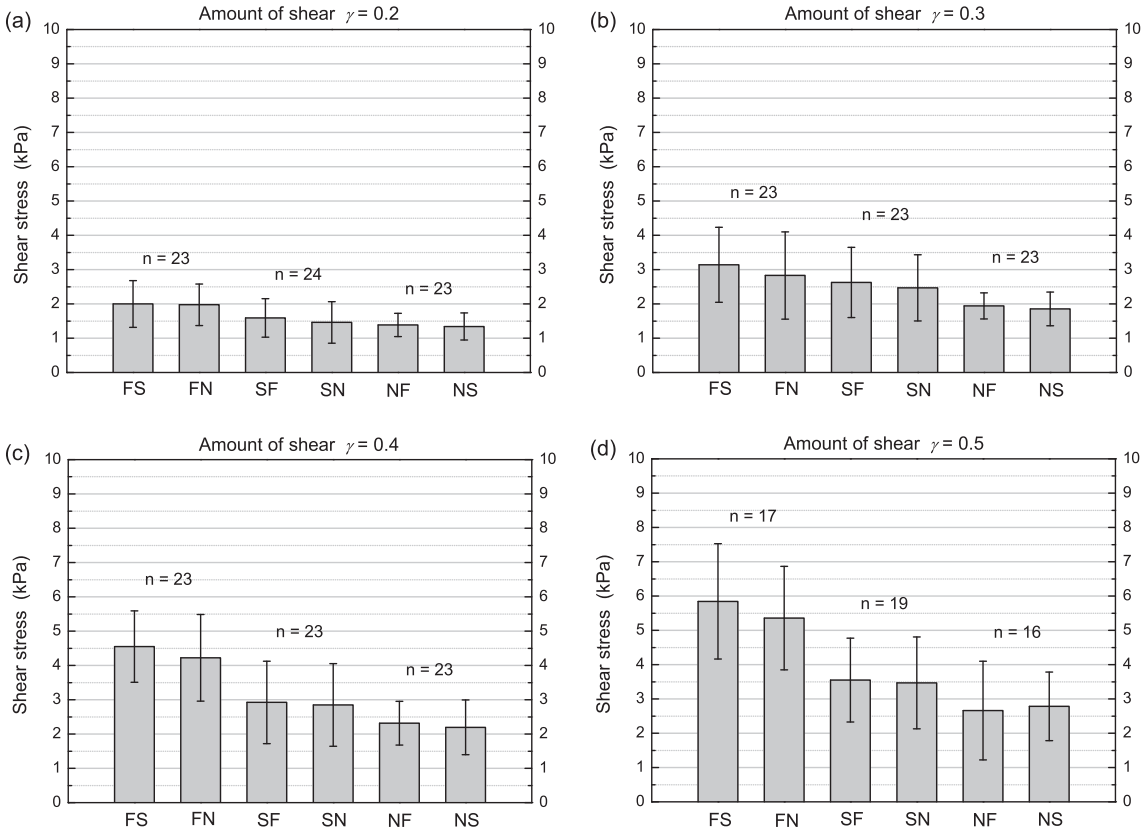


**Fig. 14.** Column plots of the peak shear stress values (mean ± SD) obtained from triaxial shear testing of human left ventricular myocardial cubes (LVFW and septum). Peak stress values for all shear modes (FS, FN, SF, SN, NF, NS) and 'amount of shear'-levels for $\gamma = 0.2$ in (a), 0.3 in (b), 0.4 in (c), and 0.5 in (d). Error bars indicate SD values. The number of specimens considered is stated above the columns.

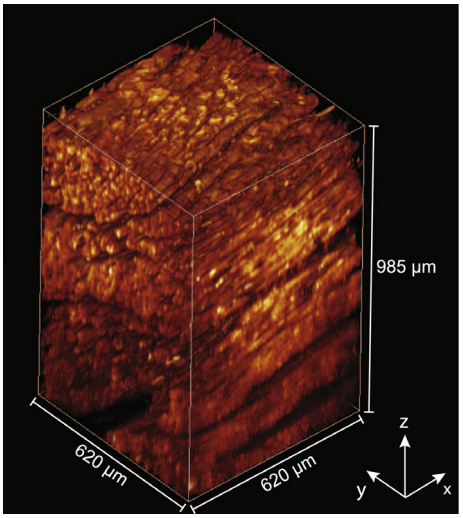


**Fig. 15.** Representation of a heart muscle fiber stack volume-rendered using the software package AMIRA. The overall depth of the depicted *z*-stack (with a step size of 5 µm between the images) is 985 µm, with an in-plane field of view of 620 × 620 µm.

stress-stretch behavior of MFD and CFD, see also Fig. 7(c), (d). This means that a 25% lower deformation of the CFD with respect to the MFD results in an almost isotropic response of the passive human myocardium.

All different regions of the human myocardium (LVFW, septum, RVFW, equatorial or apical, epicardial or endocardial) revealed similar qualitative behavior (nonlinearity, anisotropy, hysteresis formation, softening, etc.) under biaxial loadings. These qualitative results are consistent with previously published data, mostly on dogs (one leporine and one bovine study) [23–25,48,26,27,49,51]. In order to be able to quantitatively compare the different regions,

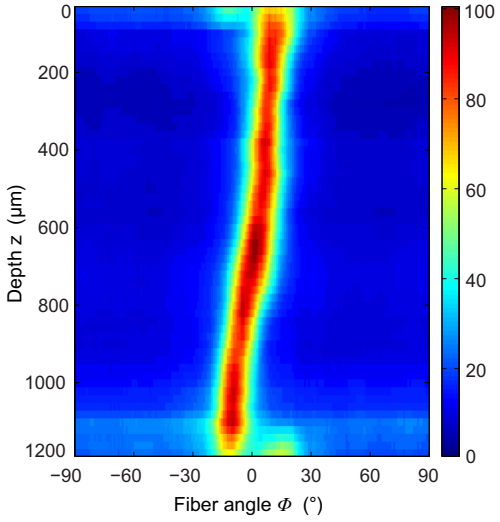


**Fig. 16.** Typical intensity plot of the three-dimensional myocyte fiber orientations through-the-thickness of 1200 µm of sample *X*. The colors ranging from dark blue (0%) to dark red (100%) correspond to the relative amplitudes of the angles displayed on the *x*-axis. Red areas show preferred fiber orientations and thus, a high density of fibers in the indicated direction, whereas blue areas display orientations with a low fiber density. (For interpretation of the references to color in this figure legend, the reader is referred to the web version of this article.)

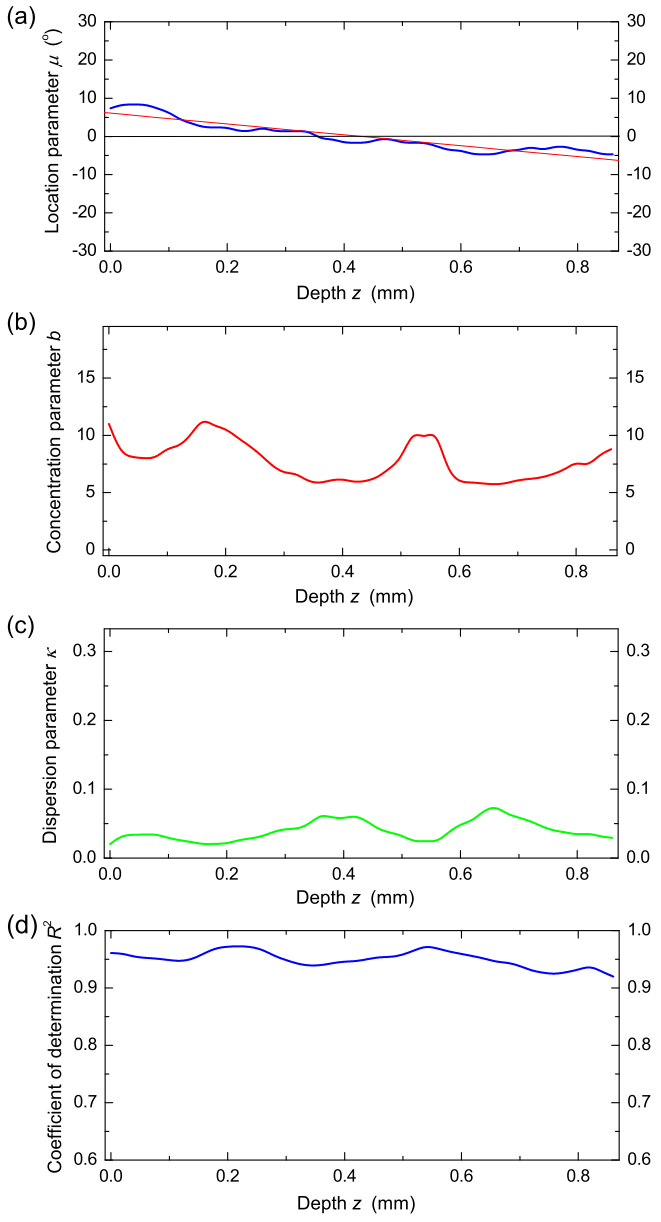


**Fig. 17.** (a) typical changes of location parameter $\mu$ (i.e. preferred fiber orientation); (b) concentration parameter $b$ (i.e. fiber alignment); (c) corresponding dispersion parameter $\kappa$; (d) coefficient of determination $R^2$ ('goodness of fit') of the myofiber orientation in the $(x,y)$-plane over a depth of 870 μm. These microstructural data were obtained from SHG investigations of sample *XIII*.

peak Cauchy stresses (mean ± SD) of equibiaxially tested myocardium at different stretch levels were calculated, see Table 3. Similar ratios between peak stress values in MFD and CFD were found in different regions. On average, we obtained an about twice as stiff human myocardium in MFD than in CFD. This corresponds well with ratios found for canine LV myocardium of 1.5–3 [25]. A generally stiffer behavior of the MFD than the CFD was also found for bovine hearts [51] and in a further study on canine hearts [27]. Furthermore, peak Cauchy stresses were similar for the LVFW and the septum, and showed no significant changes throughout the ventricular wall or from the basal to apical side. This is consistent with the similar behavior throughout the wall observed for canine, leporine, and bovine LV tissues [27,49,51]. However, we found strikingly stiffer behavior of the RVFW in comparison to the LVFW and the septum, but unfortunately, only three specimens were tested of the RVFW. Thus, it was not possible to make statistically meaningful comparisons between the mechanical features of the left and right ventricle. For the canine LV myocardium, equibiaxial Cauchy stresses in MFD and CFD at 15% stretch were determined to be approx. 1.4 and 1.1 kPa [25], 2.0 and 0.7 kPa [26] and 2.3 and 2.0 kPa [27], respectively. Slightly higher stress values, 4.9 kPa (MFD) and 2.8 kPa (CFD), were observed for the passive bovine LV myocardium [51]. However, the human LV myocardium tested herein showed clearly higher Cauchy stresses, on average $18.9 \pm 6.3$ kPa in MFD and $10.5 \pm 4.0$ kPa in CFD at the same stretch level. Due to the history-dependent (strain softening) behavior of the passive mechanical behavior of the myocardium, some of the differences could be explained by the different protocols prior applied to the tissue. Nevertheless, the big difference to animal tissue reveals the necessity of testing human tissue obtained from similar regions to identify reasonable constitutive parameters for the tissue of interest.

The stress relaxation seen during step tests and increased stresses at higher actuator speeds indicate that the human myocardium has viscoelastic properties under biaxial extension loading. It has been shown that the passive mechanical properties of skeletal muscle depend on the strain rate, in particular at the low strain rates [62]. Viscoelasticity reflects energy losses due to frictional processes such as tissue fluid movement, and is commonly observed in soft biological tissues [63,5].

In comparison, the ventricular epicardium showed a more pronounced nonlinear behavior, meaning it is initially very compliant and becomes very stiff near the limit of its extensibility with the formation of a slight hysteresis [41]. It was further shown that canine ventricular epicardium behaves like a very compliant isotropic material up to ~ 16% equibiaxial extension [41]. In contrast, human ventricular myocardium revealed stiffening and anisotropic

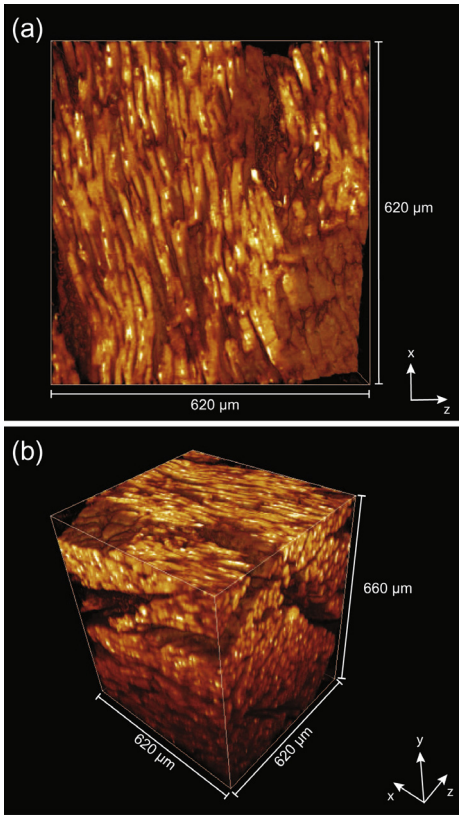


**Fig. 18.** Volume rendering of optical sections obtained by SHG imaging. Previous to the actual imaging, the sample was rotated 90° around the $x$-axis: (a) out-of-plane $(x,z)$ projection of the top of the volume-rendered sample; (b) 3D reconstruction of the image stack featuring a depth of 660 μm.

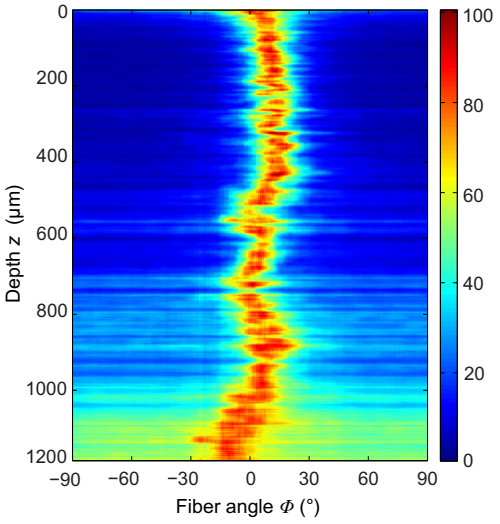


**Fig. 19.** Representative intensity plot of the muscle fiber orientations of sample *XII*, which was rotated 90° around the $x$-axis to image the $(x,z)$-planes over a depth of 1200 µm. The imaging direction is approximately coincident with the longitudinal direction of the heart. The colors ranging from dark blue (0%) to dark red (100%) correspond to the relative amplitudes of the angles displayed on the $x$-axis. Red areas show the preferred fiber orientations and thus, a high density of fibers in the indicated direction, while blue areas display orientations with a low fiber density. The slice distance between individual slices is 0.4 µm. (For interpretation of the references to color in this figure legend, the reader is referred to the web version of this article.)

behavior starting at very low stretches $\sim 2\%$, see the Figs. 7 and 8. Moreover, ventricular myocardium exhibited formation of a distinct hysteresis and strain softening, which was not observed for ventricular epicardium. This is an important observation because it speaks against treating the heart wall as a homogenous material. Furthermore, if *in vivo* epicardial stretches do not exceed stretches of $\sim 15\%$, the effect of the epicardium on the underlying myocardium might be minimal [41]. Conversely, since the epicardium gets very stiff close to its limits of extensibility, the collagenous epicardial tissue could provide resistance against acute overexpansion of the heart similar to the role of the adventitia in arteries [64,45,46].

Displacement measurements of the markers support the analytical assumption of negligibility of shear deformations and associated stresses when the specimen sites are oriented in MFD and CFD, respectively [37]. Corresponding data and analysis are not shown herein. For details the reader is referred to the preliminary study on the quantification of shear displacements and corresponding stresses of biaxially tested myocardium [37].

### 4.2. Triaxial shear behavior

Shear properties of the passive human ventricular myocardium are nonlinear, viscoelastic, and clearly dependent on the local myocardial structure. The 'amount of shear'-values applied on the human myocardium (0.1—0.5) cover the range of shear deformations reported for the beating heart [30]. Consistent with the biaxial extension behavior, passive ventricular tissue appears to be markedly resistant to shear deformations that produce extension of the myofiber axis. The stiffness along the three axes distinctly decrease from F-, over S- to the N-direction, which agrees with the observed orthotropic mechanical properties of porcine ventricular myocardium [30]. In particular, the FN and FS modes, where the predominate fiber axis gets extended, revealed the highest stiffness; the SF and SN modes showed intermediate properties, whereas the NF and NS modes, where the myocardial sheets are parallel to the top and bottom plates, exhibited the lowest stiffness. Also, *in vivo* investigations of the end-diastolic shear strains and end-systolic shear strains in the LV of dogs indicate a similar shear stiffness progression, as observed in the studies [65,66].

Similar to the biaxial extension mode, the passive cardiac muscle revealed a pronounced hysteresis loop during cyclic shear loading where the area in the center of the hysteresis loop is the energy dissipated. Interestingly, the size of the hysteresis was almost rate-independent during shearing (not shown herein). Hysteresis area or energy dissipation was more pronounced during shearing than during biaxial tension, compare the values in Tables 2 and 4. For example, hysteresis areas during simple shear testing at a low shear level of 0.2 in the FS mode (93 J/m$^3$) were even higher than for biaxial extension testing at 10% stretch in MFD (91 J/m$^3$). This suggests a higher energy dissipation during a cyclic shear loading than during a cyclic extension loading of the passive

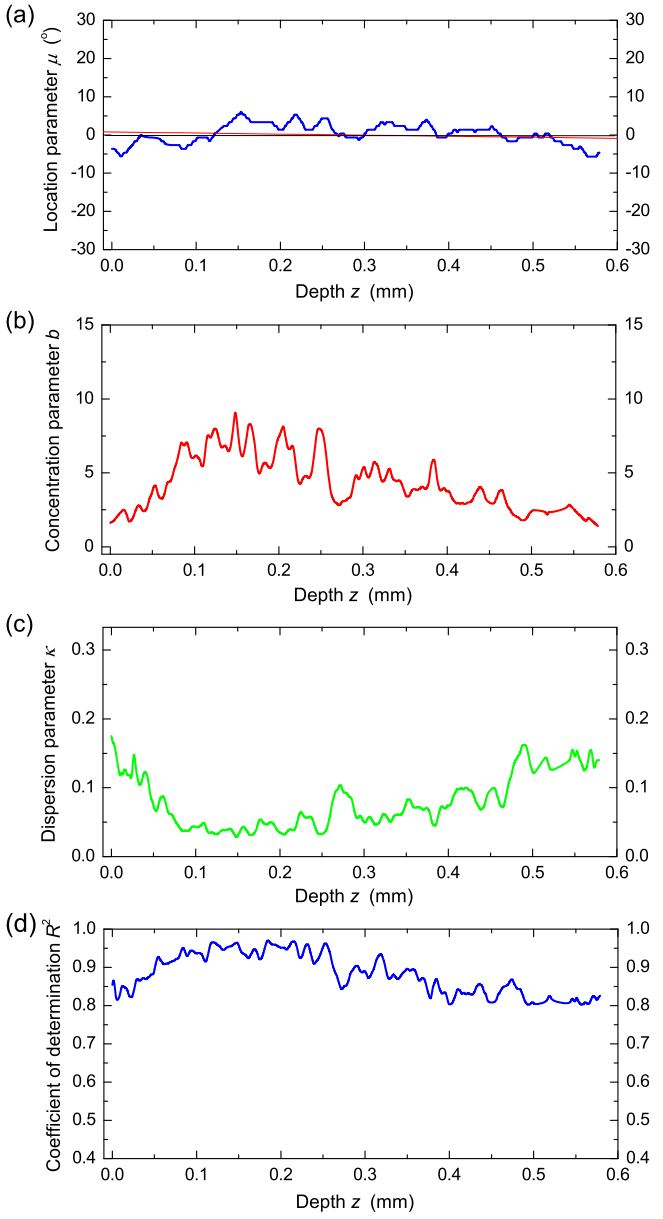


**Fig. 20.** (a) typical changes of location parameter $\mu$ (i.e. preferred fiber orientation); (b) concentration parameter $b$ (i.e. fiber alignment); (c) corresponding dispersion parameter $\kappa$; (d) coefficient of determination $R^2$ ('goodness of fit') of the myofiber orientation in the $(x,z)$-plane over a depth of 580 µm. These microstructural data were obtained from SHG investigations of the $(x,z)$-plane of sample *XII*.

**Table 2**
Average hysteresis areas, i.e. dissipation energy per unit volume, of human ventricular specimens ($n = 26$) obtained during biaxial testing at 10% stretch. In particular, for different stretch ratios the absolute hysteresis areas (J/m$^3$) and relative hysteresis areas (%) regarding the areas under the loading curve in MFD and CFD are given.

| Stretch ratios | Hysteresis area | | | |
|---|---|---|---|---|
| | MFD | | CFD | |
| | J/m$^3$ | % | J/m$^3$ | % |
| 1:1 | 91 | 38 | 52 | 38 |
| 1:0.75 | 68 | 40 | 19 | 32 |
| 0.75:1 | 29 | 34 | 32 | 38 |
| 1:0.5 | 62 | 43 | 6 | 23 |
| 0.5:1 | 8 | 29 | 26 | 40 |

myocardial tissues. This may be explained by a higher relative sliding of tissue components during shearing than during tension. According to Humphrey [5], the hysteresis is consistent with a viscoelastic response, which is related to the substantial water content (about 80% by wet weight) but also the presence of muscle. Changes in water content such as edema could therefore cause alterations in the passive stiffness and viscoelasticity of the myocardium [5]. However, the origin of the hysteresis in quasi-static loaded myocardium is currently unknown. It is known that the giant protein titin, which connects the Z line to the M line in the sarcomere, significantly contributes to the passive properties of muscle fibers while undergoing tensile deformations [61,67,62]. Furthermore, many studies have shown that titin does in fact behave viscoelastically and displays force hysteresis secondary to folding and refolding of immunoglobulin-like domains [68–71,62]. On the other hand, other researchers have argued that the actomyosin interaction might be responsible for the hysteresis formation [72,73]. All solid and liquid intra- and extra-cellular components in the myocardium will make some contributions to the hysteresis formation, but to which extent is unknown.

**Table 3**
Peak Cauchy stress values (kPa) at different stretch levels ranging from 1.05 to 1.2 in 0.25 increments obtained from equibiaxial extension testing. In particular, peak stress values (mean (SD)) corresponding to MFD and CFD for all considered specimens obtained from different regions of the human myocardium, i.e. left ventricle (LV), left ventricular free wall (LVFW), septum, right ventricular free wall (RVFW). Considered numbers of specimens ($n$) are given. Unfortunately, at higher stretch levels, Cauchy stresses were not available for the septum and for the RVFW due to failure of the tissue close to the hooks. Values are plotted in terms of column plots in Fig. 10.

| Stretches | LV | | LVFW | | Septum | | RVFW | |
|---|---|---|---|---|---|---|---|---|
| | MFD | CFD | MFD | CFD | MFD | CFD | MFD | CFD |
| 1.05 | 2.6 (1.5) | 1.3 (0.6) | 2.7 (1.7) | 1.2 (0.6) | 2.4 (1.2) | 1.6 (0.6) | 2.2 (0.7) | 1.8 (0.4) |
| | ($n = 33$) | | ($n = 24$) | | ($n = 9$) | | ($n = 3$) | |
| 1.075 | 5.1 (2.6) | 2.8 (1.3) | 5.3 (2.9) | 2.6 (1.2) | 4.6 (1.6) | 3.4 (1.5) | 6.3 (1.7) | 4.8 (0.6) |
| | ($n = 31$) | | ($n = 24$) | | ($n = 7$) | | ($n = 3$) | |
| 1.1 | 8.3 (2.3) | 4.9 (2.3) | 7.9 (3.0) | 4.7 (2.2) | 8.5 (1.9) | 5.3 (2.6) | 14.1 (1.9) | 10.8 (0.6) |
| | ($n = 26$) | | ($n = 19$) | | ($n = 7$) | | ($n = 3$) | |
| 1.125 | 12.1 (4.0) | 5.9 (1.8) | 11.4 (4.1) | 6.0 (1.8) | 13.5 (3.8) | 5.6 (1.7) | 34.8 (-) | 25.7 (-) |
| | ($n = 20$) | | ($n = 15$) | | ($n = 5$) | | ($n = 2$) | |
| 1.15 | 18.9 (6.3) | 10.5 (4.0) | 17.7 (6.9) | 10.4 (3.9) | 22.2 (2.4) | 11.1 (4.8) | – – | – – |
| | ($n = 15$) | | ($n = 11$) | | ($n = 4$) | | | |
| 1.175 | 17.4 (1.8) | 12.3 (2.6) | 17.4 (1.8) | 12.3 (2.6) | – – | – – | – – | – – |
| | ($n = 5$) | | ($n = 5$) | | | | | |
| 1.2 | 20.3 (–) | 9.4 (–) | 20.3 (–) | 9.4 (–) | – – | – – | – – | – – |
| | ($n = 2$) | | ($n = 2$) | | | | | |

Softening during shearing was observed whenever the shear level was increased, but was stabilized after only one preconditioning cycle, see Fig. 12(a). In addition, strain softening seems to be even more pronounced during shearing than during biaxial tension. Viscoelasticity cannot account for this history-dependent behavior of the passive myocardium, since unlike viscoelastic relaxation, the tissue does not recover, even after hours of rest [74]. Under passive (ischaemic, cardioplegic) conditions, strain softening is commonly observed during physiological and supra-physiological strain/loading levels in both whole hearts and small tissue blocks [55,57,30]. It is reported that strain softening behavior is absent in intact, viable (activatable) rat ventricular trabeculae [75], but becomes readily apparent once trabeculae lose viability (defined as unresponsiveness to electrical stimulation) [74]. Interestingly, strain softening was independent of the presence of BDM in rat ventricular trabeculae [74]. The cause of this behavior is presently unknown. It is hypothesized that strain softening reflects irreversible damage to passive (i.e. nonactively cycling) structure elements within the tissue that is in a state of partial or full rigor [74]. For example, damaged perimysial fibers were evident in micrographic investigations of the myocardial tissue from hearts, which had been inflated to 120 mmHg [55,57]. At extensions larger than 3 μm only, strain softening has been observed during axial extension of skinned cardiac myocytes [60] and individual cardiac myofibrils [76,77]. For extensions lower than 2.3 μm, titin showed viscoelastic softening, which fully recovered after 10 s of rest [78,69], and viable trabeculae did not exhibit strain softening [74]. It shows that (inelastic) strain softening occurs for the passive (unviable) cardiac muscle if a myofibril is axially extended greater than 3 μm, but is not observed in activated (viable) cardiac muscle. However, we observed strain softening at a very low biaxial stretch (2.5%) and 'amount of shear' (5%) (not shown herein), and it seems to increase with increasing strains, see the Figs. 7 and 11. It is possible that the softening observed at very low strains may be due to a rearrangement of the extracellular connective tissue associated with altered mechanical loadings.

The average 'elastic' stress–strain responses presented in Figs. 9, 10, 13 and 14 reflect consistent differences between orientations across all hearts. However, there was some variation in the absolute values of stress between hearts, as indicated by the error bars in these figures. The variation in the mechanical properties from heart to heart is possibly explained by variations in tissue architecture and collagen density, which naturally changes with age, gender, genetics, risk factors, etc. For example, differences in the laminar organization of myocardial cubes from heart to heart were observed. In some cases, there were regions in which the predominant layer direction was curved and not straight as ideally assumed. Furthermore, microstructural investigations indicated interheart differences in fiber dispersion.

We found a significant positive correlation between the heart-specific E/A ratio and the mechanical stiffness of the myocardium. This means that the passive stiffness of the myocardium is directly related with its E/A ratio *in vivo*. The E/A ratio, which can be easily obtained by Doppler echocardiography, is the ratio of the early (E) to late (A) ventricular filling velocities. In a healthy heart, the E velocity is greater than the A velocity. Interestingly, no significant correlations between patient data, i.e. age and ejection fraction, and mechanical properties were obtained.

### 4.3. Microstructural investigation

The novel approach of SHG microscopy combined with optical tissue clearing was used, allowing a fast and automated analysis of the cardiac tissue microstructure. The used method enables the representation of heart muscle fibers in a *z*-stack as a

**Table 4**
Hysteresis areas or dissipation energy per unit volume ($J/m^3$) observed during simple shear testing of human left ventricular myocardium for all shear modes (FS, FN, SF, SN, NF, NS) and different shear levels (0.2, 0.3, 0.4, 0.5). Values are plotted in terms of column plots in Fig. 12(b).

| Amount of shear | Shear mode | | | | | | | | | | | |
|---|---|---|---|---|---|---|---|---|---|---|---|---|
| | FS | | FN | | SF | | SN | | NF | | NS | |
| | Mean | (SD) | Mean | (SD) | Mean | (SD) | Mean | (SD) | Mean | (SD) | Mean | (SD) |
| 0.2 | 93 | (62) | 77 | (48) | 79 | (44) | 74 | (39) | 81 | (44) | 83 | (47) |
| 0.3 | 175 | (116) | 148 | (88) | 147 | (84) | 142 | (74) | 144 | (78) | 150 | (86) |
| 0.4 | 278 | (183) | 236 | (141) | 234 | (132) | 226 | (116) | 212 | (116) | 225 | (126) |
| 0.5 | 344 | (200) | 301 | (161) | 304 | (133) | 301 | (129) | 227 | (120) | 225 | (110) |

**Table 5**
Peak shear stress values (kPa) obtained from triaxial shear testing of human left ventricular myocardial cubes (LVFW, septum). Stress values (mean ± SD) corresponding to all six shear modes (FS, FN, SF, SN, NF, NS) and 'amount of shear'-levels of 0.2–0.5, in 0.1-increments. Values are plotted in terms of column plots in Fig. 14.

| Amount of shear | Shear mode | | | | | | | | | | | |
|---|---|---|---|---|---|---|---|---|---|---|---|---|
| | FS | | FN | | SF | | SN | | NF | | NS | |
| | Mean | (SD) | Mean | (SD) | Mean | (SD) | Mean | (SD) | Mean | (SD) | Mean | (SD) |
| 0.2 | 2.0 | (0.7) | 2.0 | (0.6) | 1.6 | (0.6) | 1.5 | (0.6) | 1.4 | (0.3) | 1.3 | (0.4) |
| 0.3 | 3.1 | (1.1) | 2.8 | (1.3) | 2.6 | (1.0) | 2.5 | (1.0) | 1.9 | (0.4) | 1.9 | (0.5) |
| 0.4 | 4.6 | (1.0) | 4.2 | (1.3) | 2.9 | (1.2) | 2.8 | (1.2) | 2.3 | (0.6) | 2.2 | (0.8) |
| 0.5 | 5.8 | (1.7) | 5.4 | (1.5) | 3.5 | (1.2) | 3.5 | (1.3) | 2.7 | (1.4) | 2.8 | (1.0) |

three-dimensional orientational distribution and, moreover, the determination of material parameters, which can be further used in computational modeling. The elevated resolution and specificity of SHG microscopy in contrast to clinical imaging modalities such as diffusion tensor MRI, which image through a considerably higher depth, come at the expense of limited penetration depths of 100 to 300 μm. However, the combination of SHG with optical tissue clearing eludes this drawback. As can be seen in Fig. 5, optical clearing definitely leads to an elevated transparency, and hence the penetration depth is increased severalfold [79]. Due to the optical tissue clearing performed on the samples beforehand, penetration depths ranging from 600 to 1500 μm could be achieved by means of SHG. Optical clearing does not affect the fiber orientations of tissue samples, by comparing the fiber distributions before and after the optical clearing process [35]. According to the literature, the dehydration process previous to the optical clearing was performed by a graded ethanol series in 30 min cycles for porcine hearts [80]. However, as preliminary tests showed that the dehydration process of the human myocardium improves with a slightly extended duration of the cycles, the samples stayed in the respective dilution grades for 45 mins. Exposure times longer than 45 mins, however, did not improve the results any further. After dehydration, a shrinkage of roughly 5–10% of the samples was observed. The shrinkage due to dehydration is consistent with the literature [81,80]. As the measured shrinkage of the samples is rather low and uniform in all directions, it is assumed to not affect the analysis of the structure.

Volume-rendering enabled the generation of 3D models of the image stacks obtained by SHG. Several basic similarities are visible in all 3D reconstructions, see, e.g., Figs. 15 and 18. It is obvious that cardiac muscle fibers are straight, running in parallel with one preferred fiber direction, however, deposits such as fat seem to compromise the regular and compact structure. The 3D reconstructions enable the visualization of the alignment of fibers in sheets, which, according to the literature are 3–4 cells wide [39]. Nevertheless, the sheets observable in the 3D reconstructions (see Figs. 15 and 18) seem to exceed this width. Visually, it was not possible to distinguish the samples according to their location within the heart due to their epicardial, medial or endocardial origin.

One principal (or preferred) direction of fiber orientation refers to anisotropic regions for the distribution fitting of which a von Mises distribution was used. Hence, the principal fiber orientation $\mu$ and the concentration parameter $b$, a measure of the fiber density around $\mu$, could be determined, from which the dispersion parameter $\kappa$ was calculated accordingly. These parameters can be further used in computational models to create simulations. Distribution fitting was performed through both Maximum Likelihood Estimation (MLE) and Least Squares Fitting (LSF), however, the results acquired by the latter were preferred. Due to the orientation of cardiac muscle fibers, MLE would find non-existing data beyond the peak leading to a flatter, and hence falsified distribution. Therefore, LSF was used in order to gain reasonable results. The fiber orientations illustrated in the intensity plot confirm the visual impression gained by considering the 3D reconstruction of the image stacks obtained by means of volume rendering. The cardiac muscle fibers generate high anisotropy, as indicated in the intensity plot, the preferred orientations appearing in red enclosed by dark blue areas. Bright blue or turquoise streaks, however, indicate larger isotropy as the fiber alignment is less expressed, but the dispersion increased.

Analysis of 21 myocardial samples results in an average rotation of $14.8 \pm 6.9^\circ$ per mm depth, where outliers are already omitted. These results are close to the values reported in previous studies. Histological studies have shown that the orientation of fiber angles vary from roughly $-60^\circ$ to $+60^\circ$ across the human ventricle wall [39]. Moreover, the total fiber rotation among the wall from epi- to endocardium has been reported to be $140^\circ$ in rat [82], $135^\circ$ in guinea pig [80], $140^\circ$ in dog [83], $180^\circ$ in pig [84], and $106^\circ$ in mouse [80]. Assuming the ventricle wall to be about 10–15 mm thick, the obtained results are consistent with published findings. Small differences may arise due to distinct species, however, the porcine and the human myocardium are close to identical in this regard. The relationship between the fiber angle rotation and the transmural depth throughout the ventricular myocardium was not perfectly linear, which is similar to the findings on canine and porcine myocardium documented by Streeter et al. [84,83]. In particular, they found a not perfectly linear transmural variation in the fiber angle near the endo- and epicardium, compared to the mid wall. We also obtained higher transmural fiber angle variations for the myocardial tissues close to the epicardium ($\sim 20^\circ$/mm, $n = 5$) than for the mid wall ($\sim 15^\circ$/mm, $n = 8$) and the myocardium close to the endocardium ($\sim 13^\circ$/mm, $n = 8$). To

show that the cardiac muscle fibers are organized in sheets, rectangular pieces of two heart samples were cut and rotated 90° around the $x$-axis prior to imaging. The images obtained proved that little to no fibers run in the radial (depth-) direction. The calculated rotation of the fiber direction is essentially smaller than recorded in the $(x, y)$-plane with the 3D reconstructions illustrating the organization of fibers in sheets. The out-of-plane rotation was only determined for three specimens, however, these specimens exhibited a similar rotation resulting in a mean radial rotation of only $3.5 \pm 2.0°$ per mm depth.

The LV has to support a higher pressure than the RV and thus, the wall thickness of the LV is larger. Although the RV wall is smaller, the obtained results show that the rotation across the wall is comparatively high. The fiber angle of the mid wall section of the RVFW varied smoothly with an average of $\sim 46°$/mm ($n = 2$). Assuming the RV wall to be 4 mm thick, this would lead to a change of rotation of roughly 180° throughout the wall. According to our findings, the rotation throughout the RV wall is approximately the same as throughout the LV wall, the latter being about 10–15 mm thick. This leads to a faster rotation of the muscle fiber direction through the RV. The RV has similar functions as the LV, and, therefore, the overall rotation is approximately the same. However, the small quantity of (only two) RV specimens does not allow to draw any conclusion. For the swine RVFW an abrupt jump in the fiber angle was observed when moving from the sub-epicardial to the mid wall region [85]. However, this could not be seen in our data.

The methods used provide detailed information about the myocardial microstructure due to its high resolution, and enables the visualization of the fiber alignment in sheets. Moreover, it offers the identification of structural parameters, and hence the dispersion. The dispersion parameters that can be directly used in computational modeling were determined for the human myocardium for the first time.

### 4.4. Limitations

Dissection of test specimens from the compound of the ventricle certainly released residual stresses that existed in the compound of the ventricle before specimen removal. Cutting injuries, which may occur from cutting edges during the specimen preparation, comprise the risk of compromising their structural and mechanical integrity and will have some influence to the mechanical behavior. Furthermore, there is no doubt that the deformations imposed by biaxial extension and simple shear testing differ from those experienced *in vivo*. The above-mentioned factors, besides the passiveness of the heart muscle, may also contribute to the strain softening observed in this study, and may explain the softening behavior observed at very small strains. Asymmetry of shear properties between positive and negative 'amount of shear' was commonly observed in initial tests. This was due, in part, to small relative shear displacements of upper to lower surfaces of the specimen during mounting. The residual shear was minimized by offset correction of the lower platform before testing. As already mentioned above, the structure was not completely uniform throughout the cubic specimens for shear testing. There were gradual changes in fiber and sheet orientation across each cube. This variation will inevitably blur the true extent of the differences between the material directions. The usage of samples from the mid wall, where the structure is more uniform than in the subendocardial and subepicardial regions, helped to minimize this limitation. Although the issues associated with *in vitro* mechanical testing may limit the reliability of explicit material parameter identification, the approach used here has provided important novel data on the material response of the passive human ventricular myocardium under biaxial extension and triaxial shear loading.

## 5. Conclusion

In conclusion, the results of this study suggest that the passive human LV myocardium under quasi-static and dynamic multiaxial loading can be characterized as a nonlinear, anisotropic (orthotropic), viscoelastic and history-dependent soft biological material. To our knowledge, this is the first investigation in which the mechanical properties of human ventricular tissue have been characterized under biaxial extension and triaxial shear loadings. The nonlinear and orthotropic features are consequences of the material properties of the tissue components along the local microstructural axes, i.e. myocytes, endo- and perimyosial collagen fibers in the fiber-, sheet- and sheet-normal-directions. Consequently, the passive myocardium has to be optimally modeled as a nonlinear (exponential-stiffening), orthotropic, viscoelastic and history-dependent material.

Knowledge of the biomechanical and microstructural properties of healthy and diseased tissues is necessary for comparative studies where the effect of myocardial infarction and other diseases on the mechanics of the ventricle is investigated. Moreover, these data can be used for the design of tissue engineering constructs that may successfully take over the function of impaired regions of the ventricle. These findings are important to establish and validate a general constitutive law for the passive human ventricular myocardium. The combination of advanced knowledge in heart biology and biomechanics present a special opportunity to build integrated computational models able to consider 3D patient-specific geometries, and coupling of the mechanics of the heart wall with biofluid mechanics by including cell-mediated changes in wall structure, properties, and geometry. Such computational models give a realistic chance to better understand pathological changes due to biomechanical factors and to improve, e.g., clinical diagnostics, therapeutic interventions, medical devices (e.g., pacemakers, heart valve implants), and material design for tissue engineering or drug development. The range of possible applications is huge. Of course, the goal of such efforts is to improve health care delivery and decrease the costs of our aging society.

## Acknowledgements

The authors are indebted to G. Hammer, D.C. Haspinger, R. Kresnik, M. Kutschera, S. Lind, C.A. Luttenberger, L. Marx, J. Ticar and F. Zehentner for their valuable contributions to the experimental tests. Furthermore, we gratefully acknowledge the financial support from the Austrian Science Funds (FWF) with research Grant No. P 23830-N13 to G.S., from SFB LIPOTOX F3005 to H.W. and S.D. Kohlwein, and from NAWI Graz provided to the latter. We would also particularly like to thank S.D. Kohlwein and F.R. Heinzel for their valuable support.

## References

[1] A.S. Go, D. Mozaffarian, V.L. Roger, E.J. Benjamin, J.D. Berry, M.J. Blaha, et al., Heart disease and stroke statistics – 2014 update: a report from the American Heart Association, Circulation 129 (2014) e28–e292.
[2] M. Nichols, N. Townsend, R. Luengo-Fernandez, J. Leal, A. Gray, P. Scarborough, et al., European Heart Network, European Society of Cardiology, Sophia Antipolis, Brussels, 2012.
[3] C. Gutierrez, D.G. Blanchard, Diastolic heart failure: challenges of diagnosis and treatment, Am Family Physician 69 (2004) 2609–2616.
[4] S.F. Nagueh, G. Shah, Y. Wu, G. Torre-Amione, N.M. King, S. Lahmers, et al., Altered titin expression, myocardial stiffness, and left ventricular function in patients with dilated cardiomyopathy, Circulation 110 (2004) 155–162.
[5] J.D. Humphrey, Cardiovascular Solid Mechanics. Cells, Tissues, and Organs, Springer-Verlag, New York, 2002.
[6] J.W. Holmes, T.K. Borg, J.W. Covell, Structure and mechanics of healing myocardial infarcts, Annu. Rev. Biomed. Eng. 27 (2005) 223–253.

[7] I.J. LeGrice, B.H. Smaill, L.Z. Chai, S.G. Edgar, J.B. Gavin, P.J. Hunter, Laminar structure of the heart: ventricular myocyte arrangement and connective tissue architecture in the dog, Am. J. Physiol. Heart Circ. Physiol. 269 (1995) H571–H582.
[8] H. Ashikaga, J.W. Covell, J.H. Omens, Diastolic dysfunction in volume-overload hypertrophy is associated with abnormal shearing of myolaminar sheets, Am. J. Physiol. Heart Circ. Physiol. 288 (2005) H2603–H2610.
[9] T.P. Usyk, J.H. Omens, A.D. McCulloch, Regional septal dysfunction in a three-dimensional computational model of focal myofiber disarray, Am. J. Physiol. Heart Circ. Physiol. 281 (2001) H506–H514.
[10] M.P. Nash, A.V. Panfilov, Electromechanical model of excitable tissue to study reentrant cardiac arrhythmias, Prog. Biophys. Mol. Biol. 85 (2004) 501–522.
[11] S.T. Wall, J.C. Walker, K.E. Healy, M.B. Ratcliffe, J.M. Guccione, Theoretical impact of the injection of material into the myocardium: a finite element model simulation, Circulation 114 (2006) 2627–2635.
[12] S. Niederer, L. Mitchell, N. Smith, G. Plank, Simulating a human heart beat with near-real time performance, Front. Physiol. 2 (2011) 1–7.
[13] T.S.E. Eriksson, A.J. Prassl, G. Plank, G.A. Holzapfel, Influence of myocardial fiber/sheet orientations on left ventricular mechanical contraction, Math. Mech. Solids 18 (2013) 592–606.
[14] T.S.E. Eriksson, A.J. Prassl, G. Plank, G.A. Holzapfel, Modeling the dispersion in electro-mechanically coupled myocardium, Int. J. Numer. Method Biomed. Eng. 29 (2013) 1267–1284.
[15] S. Dokos, I.J. LeGrice, B.H. Smaill, J. Kar, A.A. Young, A triaxial-measurement shear-test device for soft biological tissues, J. Biomech. Eng. 122 (2000) 471–478.
[16] G.A. Holzapfel, R.W. Ogden, Constitutive modelling of passive myocardium: a structurally based framework for material characterization, Philos. Trans. R. Soc. A. 367 (2009) 3445–3475.
[17] B. Wang, A. Borazjani, M. Tahai, A.L. Curry, D.T. Simionescu, J. Guan, et al., Fabrication of cardiac patch with decellularized porcine myocardial scaffold and bone marrow mononuclear cells, J. Biomed. Mater. Res. A 94 (2010) 1100–1110.
[18] L. Barandon, T. Couffinhal, P. Dufourcq, P. Alzieu, D. Daret, C. Deville, et al., Repair of myocardial infarction by epicardial deposition of bone-marrow-cell-coated muscle patch in a murine model, Ann. Thoracic Surg. 78 (2004) 1409–1417.
[19] R.S. Kellar, B.R. Shepherd, D.F. Larson, G.K. Naughton, S.K. Williams, Cardiac patch constructed from human fibroblasts attenuates reduction in cardiac function after acute infarct, Tissue Eng. 11 (2005) 1678–1687.
[20] A.J. Engler, S. Sen, H.L. Sweeney, D.E. Discher, Matrix elasticity directs stem cells linage specification, Cell 126 (2006) 677–689.
[21] J. Guan, F. Wang, Z. Li, J. Chen, X. Guo, J. Liao, et al., The stimulation of the cardiac differentiation of mesenchymal stem cells in tissue constructs that mimic myocardium structure and biomechanics, Biomaterials 32 (2011) 5568–5580.
[22] F. Wang, J. Guan, Cellular cardiomyoplasty and cardiac tissue engineering for myocardial therapy, Adv. Drug Deliv. Rev. 62 (2010) 784–797.
[23] L.L. Demer, F.C.P. Yin, Passive biaxial mechanical properties of isolated canine myocardium, J. Physiol. London 339 (1983) 615–630.
[24] F.C.P. Yin, R.K. Strumpf, P.H. Chew, S.L. Zeger, Quantification of the mechanical properties of noncontracting canine myocardium under simultaneous biaxial loading, J. Biomech. 20 (1987) 577–589.
[25] J.D. Humphrey, R.K. Strumpf, F.C.P. Yin, Determination of constitutive relation for passive myocardium – Part I and II, J. Biomech. Eng. 112 (1990) 333–346.
[26] M.S. Sacks, C.J. Chuong, Biaxial mechanical properties of passive right ventricular free wall myocardium, J. Biomech. Eng. 115 (1993) 202–205.
[27] V.P. Novak, F.C.P. Yin, J.D. Humphrey, Regional mechanical properties of passive myocardium, J. Biomech. Eng. 27 (1994) 403–412.
[28] M.R. Hill, M.A. Simon, D. Valdez-Jasso, W. Zhang, H.C. Champion, M.S. Sacks, Structural and mechanical adaptations of right ventricle free wall myocardium to pressure overload, Ann. Biomed. Eng. 42 (2014) 2451–2465.
[29] G.A. Holzapfel, R.W. Ogden, On planar biaxial tests for anisotropic nonlinearly elastic solids. A continuum mechanical framework, Math. Mech. Solids 14 (2009) 474–489.
[30] S. Dokos, B.H. Smaill, A.A. Young, I.J. LeGrice, Shear properties of passive ventricular myocardium, Am. J. Physiol. 283 (2002) H2650–H2659.
[31] W.J. Karlon, A.D. McCulloch, J.W. Covell, J.J. Hunter, J.H. Omens, Regional dysfunction correlates with myofiber disarray in transgenic mice with ventricular expression of ras, Am. J. Physiol. Heart Circ. Physiol. 278 (2000) H898–906.
[32] J. van der Bel-Kahn, Muscle fiber disarray in common heart diseases, Am. J. Cardiol. 40 (1977) 355–364.
[33] T. Ragan, J.D. Sylvan, K.H. Kim, H. Huang, K. Bahlmann, R.T. Lee, et al., High-resolution whole organ imaging using two-photon tissue cytometry, J. Biomed. Opt. 12 (2007) 014015.
[34] A.J. Schriefl, A.J. Reinisch, S. Sankaran, D.M. Pierce, G.A. Holzapfel, Quantitative assessment of collagen fiber orientations from 2D images of soft biological tissues, J. R. Soc. Interface 9 (2012) 3081–3093.
[35] A.J. Schriefl, H. Wolinski, P. Regitnig, S.D. Kohlwein, G.A. Holzapfel, An automated approach for 3D quantification of fibrillar structures in optically cleared soft biological tissues, J. R. Soc. Interface 10 (2013) 20120760.
[36] L.A. Mulieri, G. Hasenfuss, F. Ittleman, E.M. Blanchard, N.R. Alpert, Protection of human left ventricular myocardium from cutting injury with 2,3-butanedione monoxime, Circ. Res. 65 (1989) 1441–1449.
[37] G. Sommer, D.C. Haspinger, M. Andrä, M. Sacherer, C. Viertler, P. Regitnig, et al. Quantification of shear deformations and corresponding stresses in the biaxially tested human myocardium. Ann. Biomed. Eng. (in press), http://dx.doi.org/10.1007/s10439-015-1281-z.
[38] R.S. Kirton, A.J. Taberner, P.M. Nielsen, A.A. Young, D.S. Loiselle, Effects of BDM, $[Ca^{2+}]_o$, and temperature on the dynamic stiffness of quiescent cardiac trabeculae from rat, Am. J. Physiol. Heart Circ. Physiol. 288 (2005) H1662–H1667.
[39] D. Rohmer, A. Sitek, G.T. Gullberg, Reconstruction and visualization of fiber and laminar structure in the normal human heart from ex vivo diffusion tensor magnetic resonance imaging (DTMRI) data, Invest. Radiol. 42 (2007) 777–789.
[40] G. Sommer, M. Eder, L. Kovacs, H. Pathak, L. Bonitz, C. Mueller, et al., Multiaxial mechanical properties and constitutive modeling of human adipose tissue: a basis for preoperative simulations in plastic and reconstructive surgery, Acta Biomater. 9 (2013) 9036–9048.
[41] J.D. Humphrey, R.K. Strumpf, F.C.P. Yin, Biaxial material properties of excised ventricular epicardium, Am. J. Physiol. Heart Circ. Physiol. 259 (1990) H101–H108.
[42] T.C. Gasser, R.W. Ogden, G.A. Holzapfel, Hyperelastic modelling of arterial layers with distributed collagen fibre orientations, J. R. Soc. Interface 3 (2006) 15–35.
[43] R.B. Hickler, Aortic and large artery stiffness: current methodology and clinical correlations, Clin Cardiol. 13 (1990) 317–322.
[44] G.A. Holzapfel, G. Sommer, P. Regitnig, Anisotropic mechanical properties of tissue components in human atherosclerotic plaques, J. Biomech. Eng. 126 (2004) 657–665.
[45] G.A. Holzapfel, G. Sommer, C.T. Gasser, P. Regitnig, Determination of layer-specific mechanical properties of human coronary arteries with non-atherosclerotic intimal thickening, and related constitutive modeling, Am. J. Physiol. Heart Circ. Physiol. 289 (2005) H2048–2058.
[46] G. Sommer, P. Regitnig, L. Költringer, G.A. Holzapfel, Biaxial mechanical properties of intact and layer–dissected human carotid arteries at physiological and supra-physiological loadings, Am. J. Physiol. Heart Circ. Physiol. 298 (2010) H898–912.
[47] G. Sommer, A. Schriefl, G. Zeindlinger, A. Katzensteiner, H. Ainödhofer, A. Saxena, et al., Multiaxial mechanical response and constitutive modeling of esophageal tissues: impact on esophageal tissue engineering, Acta Biomater. 9 (2013). 9379-9091.
[48] J.D. Humphrey, R.K. Strumpf, F.C.P. Yin, Determination of constitutive relation for passive myocardium: II. Parameter estimation, J. Biomech. Eng. 112 (1990) 340–346.
[49] D.H. Lin, Yin FC.A multiaxial constitutive law for mammalian left ventricular myocardium in steady-state barium contracture or tetanus, J. Biomech. Eng. 120 (1998) 504–517.
[50] K.B. Gupta, M.B. Ratcliffe, M.A. Fallert, L.H. Edmunds Jr, D.K. Bogen, Changes in passive mechanical stiffness of myocardial tissue with aneurysm formation, Circulation 89 (1994) 2315–2326.
[51] H. Ghaemi, K. Behdinan, A.D. Spence, In vitro technique in estimation of passive mechanical properties of bovine heart part I. Experimental techniques and data, Med. Eng. Phys. 31 (2009) 76–82.
[52] P. Wang, F. Zhu, N.H. Lee, K. Konstantopoulos, Shear-induced interleukin-6 synthesis in chondrocytes: roles of E prostanoid (EP) 2 and EP3 in cAMP/protein kinase A- and PI3-K/Akt-dependent NF-$\kappa$B activation, J. Biol. Chem. 285 (2010) 24793–24804.
[53] D. Valdez-Jasso, M.A. Simon, H.C. Champion, M.S. Sacks, A murine experimental model for the mechanical behaviour of viable right-ventricular myocardium, J. Physiol. 590 (2012) 4571–4584.
[54] L. Mullins, N.R. Tobin, Theoretical model for the elastic behavior of filler-reinforced vulcanized rubbers, Rubber Chem. Technol. 30 (1957) 551–571.
[55] J.L. Emery, J.H. Omens, A.D. McCulloch, Strain softening in rat left ventricular myocardium, J. Biomech. Eng. 119 (1997) 6–12.
[56] J.L. Emery, J.H. Omens, A.D. McCulloch, Biaxial mechanics of the passively overstretched left ventricle, Am. J. Physiol. 272 (1997) H2299–H2305.
[57] J.L. Emery, J.H. Omens, O.A. Mathieu-Costello, A.D. McCulloch, Structural mechanisms of acute ventricular strain softening, Int. J. Cardiovasc. Med. Sci. 1 (1998) 241–250.
[58] D.A. MacKenna, J.H. Omens, A.D. McCulloch, J.W. Covell, Contributions of collagen matrix to passive left ventricular mechanics in isolated rat hearts, Am. J. Physiol. 266 (1994) H1007–H1018.
[59] J.B. Caulfield, T.K. Borg, The collagen network of the heart, Lab. Invest. 40 (1979) 364–372.
[60] H.L. Granzier, T.C. Irving, Passive tension in cardiac muscle: contribution of collagen, titin, microtubules, and intermediate filaments, Biophys. J. 68 (1995) 1027–1044.
[61] K. Wang, R. McCarter, J. Wright, J. Beverly, R. Ramirez-Mitchell, Viscoelasticity of the sarcomere matrix of skeletal muscles. The titin-myosin composite filament is a dual-stage molecular spring, Biophys. J. 64 (1993) 1161–1177.
[62] M.R. Rehorn, A.K. Schroer, S.S. Blemker, The passive properties of muscle fibers are velocity dependent, J. Biomech. 47 (2014) 687–693.
[63] Y.C. Fung, Biomechanics, Mechanical Properties of Living Tissues, second ed., Springer-Verlag, New York, 1993.
[64] C.A.J. Schulze-Bauer, P. Regitnig, G.A. Holzapfel, Mechanics of the human femoral adventitia including high-pressure response, Am. J. Physiol. Heart Circ. Physiol. 282 (2002) H2427–H2440.

[65] K.D. Costa, Y. Takayama, A.D. McCulloch, J.W. Covell, Laminar fiber architecture and three-dimensional systolic mechanics in canine ventricular myocardium, Am. J. Physiol. 276 (1999) H595–H607.
[66] Y. Takayama, K.D. Costa, J.W. Covell, Contribution of laminar myofiber architecture to load-dependent changes in mechanics of LV myocardium, Am. J. Physiol. Heart Circ. Physiol. 282 (2002) H1510–H1520.
[67] T. Toursel, L. Stevens, H. Granzier, Y. Mounier, Passive tension of rat skeletal soleus muscle fibers: effects of unloading conditions, J. Appl. Physiol. 92 (2002) 1465–1472.
[68] M.S. Kellermayer, S.B. Smith, C. Bustamante, H.L. Granzier, Complete unfolding of the titin molecule under external force, J. Struct. Biol. 122 (1998) 197–205.
[69] M.S. Kellermayer, S.B. Smith, C. Bustamante, H.L. Granzier, Mechanical fatigue in repetitively stretched single molecules of titin, Biophys. J. 80 (2001) 852–863.
[70] D. Labeit, K. Watanabe, C. Witt, H. Fujita, Y. Wu, S. Lahmers, et al., Calcium-dependent molecular spring elements in the giant protein titin, Proc. Nat. Acad. Sci. USA 100 (2003) 13716–13721.
[71] J. Nedrud, S. Labeit, M. Gotthardt, H. Granzier, Mechanics on myocardium deficient in the N2B region of titin: the cardiac-unique spring element improves efficiency of the cardiac cycle, Biophys. J. 101 (2011) 1385–1392.
[72] M. Linari, L. Lucii, M. Reconditi, M.E. Casoni, H. Amenitsch, S. Bernstorff, et al., A combined mechanical and X-ray diffraction study of stretch potentiation in single frog muscle fibres, J. Physiol. 526 (2000) 589–596.
[73] D.E. Rassier, W. Herzog, Considerations on the history dependence of muscle contraction, J. Appl. Physiol. 96 (2004) 419–427.
[74] R.S. Kirton, A.J. Taberner, P.M.F. Nielsen, A.A. Young, D.S. Loiselle, Strain softening behaviour in nonviable rat right-ventricular trabeculae, in the presence and the absence of butanedione monoxime, Exp. Physiol. 89 (2004) 593–604.
[75] R.S. Kirton, A.J. Taberner, A.A. Young, P.M.F. Nielsen, D.S. Loiselle, Strain softening is not present during axial extensions of rat intact right ventricular trabeculae in the presence or absence of 2,3-butanedione monoxime, Am. J. Physiol. Heart Circ. Physiol. 286 (2004) H708–H715.
[76] W.A. Linke, V.I. Popov, G.H. Pollack, Passive and active tension in single cardiac myofibrils, Biophys. J. 67 (1994) 782–792.
[77] W.A. Linke, M.L. Bartoo, M.A. Ivemeyer, G.H. Pollack, Limits of titin extension in single cardiac myofibrils, J. Muscle Res. Cell Motil. 17 (1996) 425–428.
[78] M. Helmes, K. Trombitás, T. Centner, M. Kellermayer, S. Labeit, W.A. Linke, et al., Mechanically driven contour-length adjustment in rat cardiac titin's unique N2B sequence: titin is an adjustable spring, Circ. Res. 84 (1999) 1339–1352.
[79] P. Campagnola, Second harmonic generation imaging microscopy: applications to diseases diagnostics, Anal. Chem. 83 (2011) 3224–3231.
[80] R.M. Smith, A. Matiukas, C.W. Zemlin, M. Pertsov, Nondestructive optical determination of fiber organization in intact myocardial wall, Microsc. Res. Tech. 71 (2008) 510–516.
[81] A. Cheng, F. Langer, F. Rodriguez, J.C. Criscione, G.T. Daughters, D.C. Miller, et al., Transmural sheet strains in the lateral wall of the ovine left ventricle, Am. J. Physiol. Heart Circ. Physiol. 289 (2005) 1234–1241.
[82] A.J. Pope, G.B. Sands, B.H. Smaill, I.J. LeGrice, Three-dimensional transmural organization of perimysial collagen in the heart, Am. J. Physiol. Heart Circ. Physiol. 295 (2008) H1243–H1252.
[83] D.D. Streeter Jr, H.M. Spotnitz, D.P. Patel, J. Ross Jr, E.H. Sonnenblick, Fibre orientation in the canine left ventricle during diastole and systole, Circ. Res. 24 (1969) 339–347.
[84] D.D. Streeter Jr, D.L. Basset, An engineering analysis of myocardial fiber orientation in pig's left ventricle in systole, Anat. Rec. 155 (1966) 503–511.
[85] F.J. Vetter, S.B. Simons, S. Mironov, C.J. Hyatt, A.M. Pertsov, Epicardial fiber organization in swine right ventricle and its impact on propagation, Circ. Res. 96 (2005) 244–251.